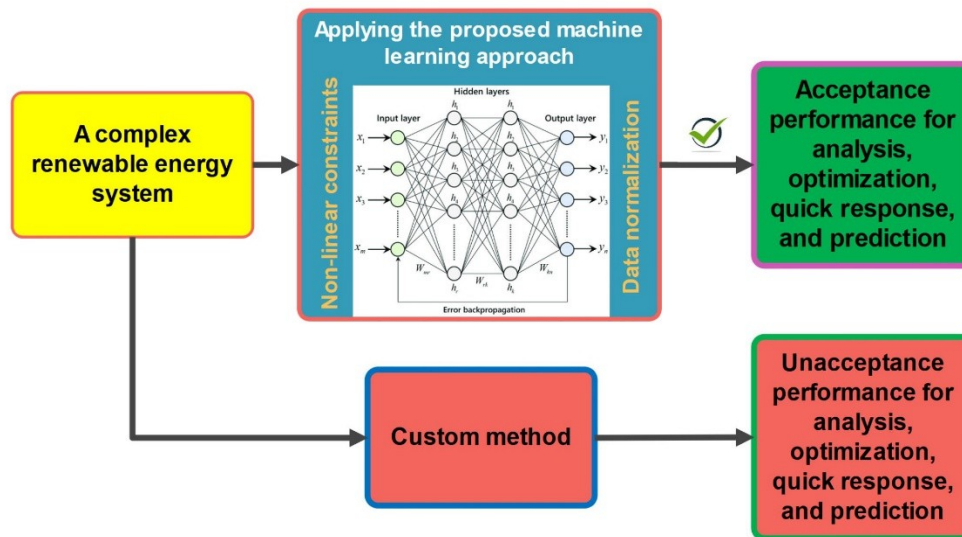


A comprehensive proposed machine learning approach for behaving complex renewable energy problems and rapid response applications; a 4E analysis and optimization study for a parabolic trough solar collector

Graphical abstract:



Abstract

Despite some advances in prospective renewable energy systems, there are still abundant obstacles against rapid development and promotion for academic research and industrial applications, including complex systems and governed equations, high solution time, and comprehensive quick response. Thus, a comprehensive and extendable machine learning-based approach is proposed in order to achieve process simplification, quick response, less energy consumption, and more precision. The process and sequences of the method were presented in detail, it is applied to a renewable energy complex problem, and it is utilizable for other similar complex problems. In the present article, a general MATLAB code was generated for 4E analysis of a parabolic trough solar collector, including energy, exergy, economic, and environmental analysis. Proper input data was generated with Minitab, increased to a sufficient volume, and pre-processing and scaling were performed. Then, through the presented machine learning approach, an accurate model was trained in order to analyze conveniently, simple prediction and optimization, prompt reaction, and implement sensitivity analysis and other requirements. In the wake of applying the presented approach, 1143 times faster response and calculation resulted as one of the achievements, which made it substantially more convenient for the analysis process and optimization. An optimization

was implemented in a simple way by the trained model by Genetic algorithm and revealed the optimum categorical and continuous variables during very low calculation, very quick time, and extremely accurate. Additionally, a sensitivity analysis and a comprehensive parametric study were executed by the trained model in a substantially convenient way for all input variables for five objective functions, including energy, exergy, heat cost, energy based emission cost, and exergy based emission cost.

1. Introduction

Renewable energy is now widely regarded as the most effective way to reduce combat global warming, fossil fuel consumption, and survive in a more sustainable environment. Renewable energy's quota is 2351 GW or thirty-three percent of the total required energy. Based on data that reported from the Agency of International Renewable Energy, the capacity of renewable increase is still being driven chiefly by wind solar energy projects. Solar energy, specially, expanded by 24%, 171GW, in 2018, demonstrating the widespread acceptance of its utilization in various applications [1].

One of the important, well-known and promising renewable energy technologies is the utilization of parabolic trough solar collectors (PTSC) to generate steam for electricity production with an Organic cycle, Rankine cycle, or Brayton cycle [2] or to transform solar irradiation into usable process heat [3]. The PTSC is made up of three primary components: a reflector, an absorber, and a working fluid (WF). The trough includes an aluminum surface or polished envelope with a reflectance of 95 or 88.5%, respectively [4]. To raise the temperature of the HTF, radiation that strikes the surface of mirror is reflected onto an absorber pip that is positioned at the focal axis of the parabola. Depending on the application, the HTF, which may be water, thermal fluids, molten salt, therminols, or gas pumped through the absorber tube, absorbs the energy and exergy from the receiver and reaches temperatures of up to 390 °C [4].

There are several different PTCS setups that are used for power plants or heating and cooling systems. These configurations vary depending on some of the impacts, such as the kind of integration, the absorber's composition and form, the working fluid, the thermal storage system, and the reflector and tracking system types [5,6].

The performance and efficiencies have a substantial engagement to the parameters as mentioned above. It is confirmed that to approach a high performance for PTSC, optimization methods are necessary procedures [6].

However, optimizing the various real-time input variable manipulation to enhance the efficiencies of PTC systems is one of the primary issues. The operating conditions, materials' properties, receiver and HTF type, and concentrator and apparatus geometry, among other things, having an

impact on performance of PTC [7]. Numerous research have centered on determining PTC systems' thermodynamic behavior utilizing computational models and simulation technologies like machine learning, particularly artificial neural networks (ANN) [8]. The experimental systems are limited by the high costs of operational and maintenance and are time-consuming. The benefits of simplicity, speed, and the capacity to handle non-linear and complex interactions between inputs and variables make ANN simulation tools and its derivatives such a promising solution for complex data processing [9].

Evolutionary Methods (EMs) like the Vector Evaluated Genetic Algorithm (VEGA) and Particle Swarm Optimization are two common AI methods for resolving Multi Objective Optimization Problems (MOPs) (PSO). After intelligent tools are available, the Particle Swarm Optimization (PSO) domain gives rise to Multi Objective Swarm Particle Optimization (MOSPO) [10]. There are two different forms of multi-objective optimization problems (MOPs): linear and nonlinear, as well as convex and non-convex. When all objective functions and constraints are linear, linear MOP is taken into account, whereas non-linear MOP is taken into account when any objective function or constraint function is nonlinear. Convex and feasible regions are taken into account while considering convex MOP, and non-convex and feasible regions are taken into account when considering non-convex MOP [11].

A numerical simulation was run to examine the effect of twisted tape inserts on the parabolic trough collector's absorber tube's circumferential temperature differential reduction and augmentation of heat transmission. The maximum circumferential temperature differential will drop by around 10–45%, the Nusselt number will increase by 1–1.7 times, the friction factor will rise by 1–4 times, and this will greatly lessen thermal stresses in the absorber tube [12].

According to the outcomes of an exergy-economic analysis of a commercial parabolic trough collector (PTSC), the exergy efficiency is 14.1% for the greatest total solar radiation of 665 W/m² in Tehran, Iran, and the exergy dissipation rate is 0.1856 kW/\$ [13].

By using an economic lens, the impact of climatic variations on a PTSC's energy, exergy, and environmental impacts was examined. The PTSC was tested in 5 Iranian cities to simulate different climates: Rasht, Shiraz, Tehran, Abadan, and Sanandaj. According to the findings of this study, Shiraz, which has a Mediterranean climate, has the parabolic solar collectors with the best thermal energy efficiency among these cities, up to 71.97% [14].

Some papers tried to assess neural network concepts alongside other analysis in the renewable energy field, but the assessments are very limited and they had a very brief glance at machine learning next to other analysis. On the other hand, high solution, optimization, analysis, and response times are the other obstacles to

academic research and industrial application. In the current study, a detailed machine learning approach is presented comprehensively to overcome the hindrances and utilize the procedure for the research and industrial application. The sequences of the method are illustrated and described, which it is extendable and could be used for other complex renewable energy problems. Herein, the analysis and optimization of energy, exergy, heat cost, energy based emission cost, and exergy based emission cost are implemented for a complex renewable energy system based on the proposed machine learning approach with detailed required tools and techniques, which is utilizable for other systems. Table 1 presents the study gaps and comparisons with the literature review.

Table 1: Gap study and comparison of the present article with literature review

| Reference | Field | Optimization | Neural network | Detailed machine learning approach | Illustrating the process and sequences to expandability | Demonstrate the applicability of the method for applying to other regions |
|-----------------|--|--------------|----------------|------------------------------------|---|---|
| [8] | Heat Transfer | ✓ | — | — | — | — |
| [15] | Thermodynamics | ✓ | — | — | — | — |
| [16] | Bioinformatics | — | ✓ | — | — | — |
| [17] | Thermodynamics | ✓ | ✓ | — | — | — |
| [18] | Thermodynamics | ✓ | ✓ | — | — | — |
| [19] | Thermodynamics | ✓ | ✓ | — | — | — |
| [16] | Thermodynamics | ✓ | ✓ | — | — | — |
| Present article | Heat transfer, Thermodynamics and hydrodynamic | ✓ | ✓ | ✓ | ✓ | ✓ |

2. System description

The schematic diagram, system description, and components of the PTSC are illustrated in Figure 1. The components of a related operating system may include a PTSC, a pump, a storage tank or heat exchanger, a flow meter, a DC-motor, piping, a heat transfer fluid, temperature and pressure sensors, a data logger, and a computer.

The HTF gains thermal heat through an absorber pipe, then the high-temperature HTF flows to a storage tank to save energy. The energy reservoir could be consumed at the same time or whenever needed. The storage tank can also derive another HTF through a heat exchanger to other aims, such as providing required heat energy for a Rankin Cycle, absorption refrigerant cycle, domestic hot

water, etc. A computer can detect the thermal properties and hydrodynamic parameters of the HTF and environmental data by data logger and temperature and pressure sensors. The computer can also control the HTF mass flow rate and the angle of the trough to increase efficiencies. Despite A number of parallel and series PTSCs, with various range of length and HTFs, could be utilized, the main cause is applying a proposed machine learning approach to simplification of the complex heat transfer part. Thus, the main concentration is on absorber part of the PTSC, which investigated in an abundant detail in following sections.

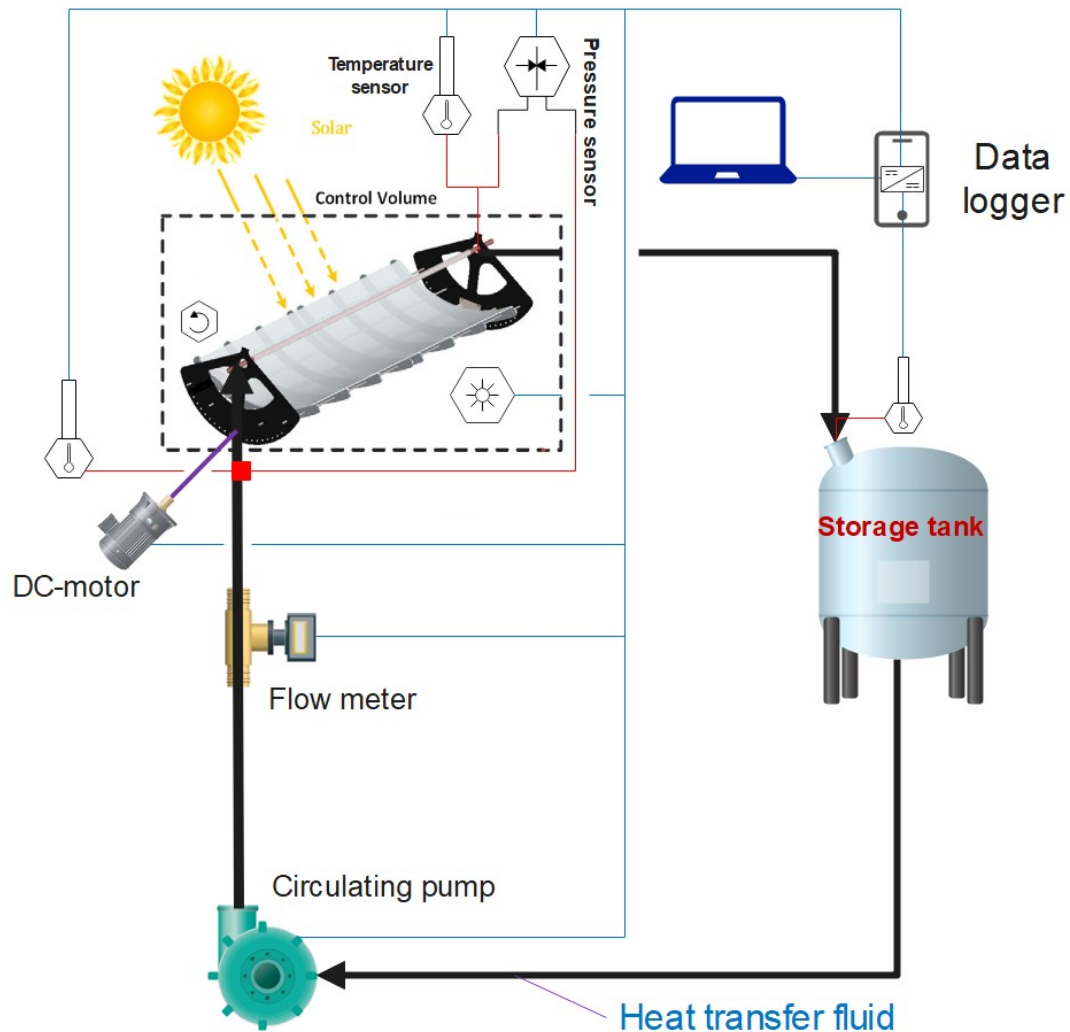


Figure 1: The schematic diagram, system description, and components of the PTSC

3. Methodology and mathematical analysis

3.1.1. Optical modeling

The number of minutes that separate solar time from standard time is [20]:

$$T_{ST} - T_l = 4\lambda \quad (1)$$

Where the T_{ST} and T_l are the solar time and local time, respectively, L_{st} is the local standard time meridian and L_{loc} is the site longitude, and E is the time equation which is computed by the Following equation [20]:

$$E = 229.2(0.000075 + 0.001868 \cos \beta - 0.032077 \sin \beta - 0.014615 \cos 2\beta) \quad (2)$$

$$\text{Where } \beta = \frac{360(n-1)}{365}$$

where n is the corresponding day of the year ($1 \leq n \leq 365$), and on first of January, $n = 1$.

For a horizontal surface, the angle at sunset is represented as [20]:

$$\omega = \cos^{-1}(-\tan \varphi \tan \delta) \quad (3)$$

Where φ and δ are, respectively, the deflection and latitude angle. The solar deflection angle in degrees could be calculated using δ [21]:

$$\delta = 23.45 \sin \left(\frac{360(284+n)}{365} \right) \quad (4)$$

3.1.2. Pressure drop in pip

The pressure drop of flow through the absorber could be calculated to:

$$\Delta P = f_{Darcy} \frac{L}{D_2} \frac{V_1^2}{2g} \quad (5)$$

With

$$V_1 = \frac{4\dot{m}}{\rho \pi D_2^2} \quad (6)$$

Where ΔP is pressure drop, L is absorber length, D_2 is absorber diameter, g is gravity constant, V_1 is mean velocity in absorber tube, \dot{m} is mass flow and ρ is fluid density.

The f_{Darcy} for laminar flow is equal to:

$$f_{Darcy} = \frac{64}{\Re_{D2}} \quad (7)$$

Where \Re_{D2} is Reynolds number of absorber tube.

And $f = f_{Darcy}/4$ for turbulent can be estimated by following equation [22]:

$$\frac{1}{\sqrt{f}} = -2 \log \left(\frac{\varepsilon/D_2}{3.7} + \frac{2.51}{\Re_{D_2} \sqrt{f}} \right) \quad (8)$$

Where f is friction factor and ε is equivalent roughness which for drawn pipe is usually equal to 1.5e-6 m.

3.2. Thermal modeling

The HCE performance model incorporates the equations and correlations required to forecast the terms in the energy balance that associate the collector type, HCE circumstances, optical qualities, and environmental conditions. It applies an energy balance between the HTF and the surroundings.

By preserving energy balance at each surface of the HCE cross-section, the four energy balance equations are established:

$$\dot{q}'_{12 \text{ conv}} = \dot{m} c (T_{outlet} - T_{inlet}) \quad (9)$$

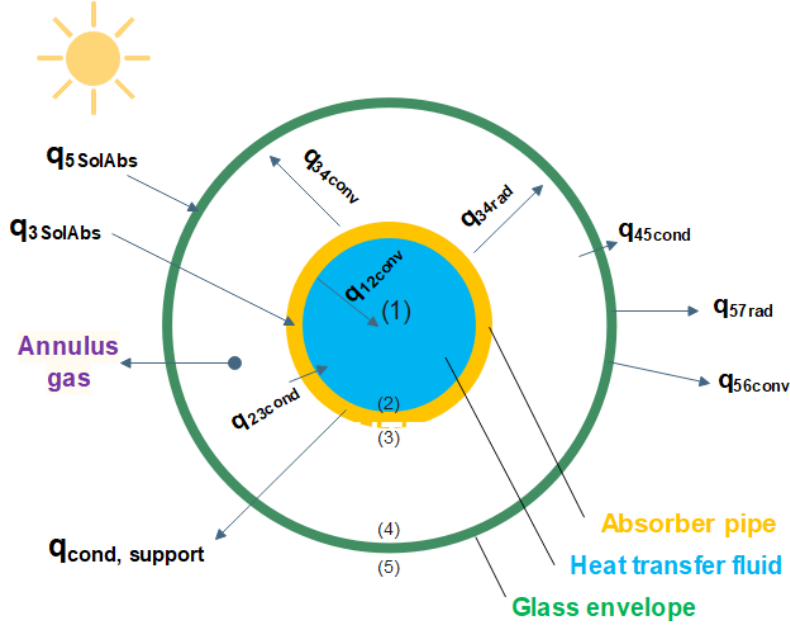
$$\dot{q}'_{12 \text{ conv}} = \dot{q}'_{23 \text{ cond}} \quad (10)$$

$$\dot{q}'_{3 \text{ SolAbs}} = \dot{q}'_{34 \text{ conv}} + \dot{q}'_{34 \text{ rad}} + \dot{q}'_{23 \text{ cond}} + \dot{q}'_{\text{cond, bracket}} \quad (11)$$

$$\dot{q}'_{34 \text{ conv}} + \dot{q}'_{34 \text{ rad}} = \dot{q}'_{45 \text{ cond}} \quad (12)$$

$$\dot{q}'_{45 \text{ cond}} + \dot{q}'_{5 \text{ Soldos}} = \dot{q}'_{56 \text{ conv}} + \dot{q}'_{57 \text{ rad}} \quad (13)$$

Where T_{outlet} is outlet temperature of HTF and T_{inlet} is inlet temperature of HTF. The absorber cross section is showed in Figure 2, where the heat fluxes are defined and specified in each surface and related components are defined.



$q_{12\text{conv}}$: Convection heat transfer from absorber inner surface to the HTF (2→1)

$q_{5\text{SolAbs}}$: Solar irradiation absorption from the incident solar irradiation to the outer glass envelope surface (s→5)

$q_{3\text{SolAbs}}$: Solar irradiation absorption from the incident solar irradiation to the outer absorber pipe surface (s→3)

$q_{23\text{cond}}$: Conduction heat transfer from the absorber outer surface to the absorber inner surface (3→2)

$q_{42\text{conv}}$: Convection heat transfer from the absorber outer surface to the envelope inner surface (3→4)

$q_{42\text{rad}}$: Radiation heat transfer from the absorber outer surface to the envelope inner surface (3→4)

$q_{45\text{cond}}$: Conduction heat transfer from the envelope inner surface to the envelope outer surface (4→5)

$q_{56\text{conv}}$: Convection heat transfer from the envelope outer surface to the ambient (5→6)

$q_{57\text{rad}}$: Radiation heat transfer from the envelope outer surface to the sky (5→7)

Figure 2: Absorber cross section, various zones and temperatures

3.2.1. Convection Heat Transfer between fluid and receiver

In the balance equations, $\dot{q}'_{12\text{ conv}}$ is the heat transmission by convection from the interior of the absorber pipe to the fluid, and it is also equals to [23]:

$$\dot{q}'_{12\text{ conv}} = h_1 D_2 \pi (T_2 - T_1) \quad (14)$$

With

$$h_1 = Nu_{D2} \frac{k_1}{D_2} \quad (15)$$

Where D_2 is the inner diameter of the absorber pipe at point 2, T_2 is the inside surface temperature of the absorber pipe at point 1, T_1 is the mean

bulk temperature of the fluid at point 1, Nu_{D_2} is the Nusselt number based on D_2 at point 1, and k_1 is the thermal conductance of the fluid at T_1 of point 1.

3.2.1.1. Modeling of turbulent and transitional flow cases

The following Nusselt number correlation [24] is used to represent the convective heat transfer from the absorber to the fluid for turbulent and transitional scenarios, Reynolds number greater than 2300:

$$Nu_{D_2} = \frac{f_2/8 (\Re_{D_2} - 1000) Pr_1}{1 + 12.7 \sqrt{f_2/8} (Pr_1^{2/3} - 1)} \left(\frac{Pr_1}{Pr_2} \right)^{0.11} \quad (16)$$

with

$$f_2 = \left(1.82 \log_{10} (\Re_{D_2}) - 1.64 \right)^{-2} \quad (17)$$

3.2.1.2. Laminar flow cases

When the flow regime is laminar, Reynolds number less than 2300, the Nusselt number will be constant and equal to 4.36 [25].

3.2.2. Conduction heat transfer through receiver thickness

The conduction heat transmission through the absorber wall is presented as occurring through a hollow cylinder [25]:

$$\dot{q}'_{23\text{cond}} = 2 \pi k_{23} (T_2 - T_3) / \ln (D_3/D_2) \quad (18)$$

Where k_{23} is the thermal conductance of the absorber at its average temperature, T_2 and T_3 are the surface temperatures within and outside of the absorber, respectively, and D_2 and D_3 are the diameters of the absorber.

3.2.3. Heat transfer from the absorber to the glass pip

The annulus pressure affects the convection heat transfer process. Molecular conduction is the primary method of heat transport at low pressures, typically less than 1 torr. Free convection is the mechanism at pressures above about 1 torr. The temperature difference between the inner glass envelope surface and the inner absorber surface causes the radiation heat transfer to occur. By assuming that the glass envelope is opaque to infrared radiation and that the surfaces are gray, the calculation for radiation heat transfer is made simpler.

3.2.3.1. Convection Heat Transfer

3.2.3.1.1. Vacuum in Annulus

Free-molecular convection is used to transport convection heat between the absorber and glass pip when the HCE annulus is under a vacuum of less than or around 1 torr [26]:

$$\dot{q}'_{34conv} = \pi D_3 h_{34} (T_3 - T_4) \quad (19)$$

With

$$h_{34} = \frac{k_{std}}{\left(D_3 / 2 \ln \left(D_4 / D_3 \right) + b \lambda \left(D_3 / D_4 + 1 \right) \right)} \quad (20)$$

$$b = \frac{(2-a)(9\gamma-5)}{2a(\gamma+1)} \quad (21)$$

$$\lambda = \frac{2.331 E(-20) (T_{34} + 273.15)}{(P_a \delta^2)} \quad (22)$$

3.2.3.1.2. Pressure in Annulus

Natural convection is used to transport heat from the absorber to the glass pip even if the HCE annulus is no longer in a vacuum condition of larger than 1 torr or so. The following equation is utilized as a result [23].

$$\dot{q}'_{34conv} = \frac{2.425 k_{34} (T_3 - T_4) (Pr Ra_{D3} (0.861 + Pr_{34}))^{1/4}}{\left(1 + (D_3 / D_4)^{3/5} \right)^{5/4}} \quad (23)$$

$$Ra_{D3} = \frac{g \beta (T_3 - T_4) D_3^3}{\alpha \nu} \quad (24)$$

For an ideal gas

$$\beta = \frac{1}{T_{avg}} \quad (25)$$

Where β is volumetric thermal expansion coefficient and T_{34} is average temperature of T_3 and T_4 .

3.2.3.2. Radiation heat transfer between absorber and glass pip

The following equation is used to determine the radiation heat transfer between the absorber and glass pip [25].

$$\dot{q}'_{34rad} = \frac{\sigma \pi D_3 (T_3^4 - T_4^4)}{\left(1/\varepsilon_3 + (1-\varepsilon_4) D_3 / (\varepsilon_4 D_4) \right)} \quad (26)$$

Where σ is Stefan-Boltzmann constant $\left(5.672 \times 10^{-8} \frac{W}{m^2 K^4}\right)$, ε_3 is emissivity of selected Absorber coating, ε_4 is emissivity of glass envelope.

3.2.4. Conduction heat transfer through the glass pip

Similar to the conduction through the absorber wall discussed in Section 3.2.2, the conduction heat transfer through the glass pip is calculated using the same equation. The temperature distribution is taken to be linear, much like in the absorber example. With a value of 1.04, the thermal conductance is considered to be constant [23].

3.2.5. Heat transfer from the glass pip to the ambient

Convection and radiation are the two way used to transfer heat between the environment and the glass enclosure. The convection will be forced or natural based on whether there is wind or not. Heat is lost by radiation when there is a temperature differential between the sky and the glass enclosure.

3.2.5.1. Convection heat transfer

A primary source of heat loss is the convection heat transfer from the glass envelope to the atmosphere, particularly when there is a breeze.

$$\dot{q}'_{56 conv} = h_{56} \pi D_5 (T_5 - T_6) \quad (27)$$

$$h_{56} = \frac{k_{56}}{D_5} Nu_{D5} \quad (28)$$

3.2.5.1.1. No wind condition

Natural convection will be used to transport convection heat from the glass pip to the environment if there is no wind or just very little wind [25]:

$$Nu_{D5} = \left\{ 0.60 + \frac{0.387 Ra_{D5}^{1/6}}{\left[1 + (0.559/Pr_{56})^{9/16} \right]^{1/4}} \right\}^2 \quad (29)$$

$$Ra_{D5} = \frac{g \beta (T_5 - T_6) D_5^3}{(\alpha_{56} \nu_{56})} \quad (30)$$

$$\beta = \frac{1}{T_{56}} \quad (31)$$

$$Pr_{56} = \frac{\nu_{56}}{\alpha_{56}} \quad (32)$$

Where Pr_{56} is the Prandtl number for air at T_{56} , ν_{56} is the kinematic viscosity for air at T_{56} , T_{56} is the mean film temperature at $(T_5 + T_6)/2$, and Ra_{D5} is the Rayleigh number for air based on the outer diameter of the glass envelope, the gravitational constant, and the thermal diffusivity for air at T_{56} . This association holds true for $10^5 < Ra_{D5} < 10^{12}$ values.

3.2.5.1.2. Wind condition

Forced convection will be used to transfer heat from the glass envelope to the environment if there is wind with a wind speed of more than 0.1 m/s or such [25].

$$\bar{N}u_{D5} = C \Re_{D5}^m Pr_6^n \left(\frac{Pr_6}{Pr_5} \right)^{1/4} \quad (33)$$

For $Pr \geq 10$ $n = 0.36$, and for $Pr \leq 10$ $n = 0.37$. This link holds true for the values of $0.7 < Pr_6 < 500$ and $1 < Re_D < 10^6$. Except for Pr_6 , which is assessed at the glass pip outer surface temperature, all fluid parameters are estimated at the ambient temperature, T_6 .

3.2.5.2. Radiation heat transfer between glass pip and ambient

The temperature differential between the glass enclosure and the sky is what causes the radiation transmission [25].

$$\dot{q}'_{57rad} = \sigma D_5 \pi \varepsilon_5 (T_5^4 - T_7^4) \quad (34)$$

Where σ is Stefan-Boltzmann constant, ε_5 is emissivity of the outer surface of glass pip and T_7 is effective sky temperature. It is estimated that the effective sky temperature is $8^\circ C$ below the surrounding temperature [27].

3.2.6. Solar irradiation absorption

3.2.6.1. Solar irradiation absorption in the glass pip

$$\dot{q}'_{5\text{ SolAbs}} = \dot{q}'_{si} \eta_{env} \alpha_{env} \quad (35)$$

with

$$\eta_{env} = \varepsilon'_1 \varepsilon'_2 \varepsilon'_3 \varepsilon'_4 \varepsilon'_5 \varepsilon'_6 \rho_{cl} K \quad (36)$$

Where \dot{q}'_{si} is solar radiation per receiver length, η_{env} is efficiency of effective optical at the glass envelope and α_{env} is the absorptance glass envelope. ε'_1 is HCE Shadowing, ε'_2 is Tracking Error, ε'_3 is Geometry Error, ε'_4 is Dirt on

Mirrors, ε_5' is Dirt on HCE, ε_6' is Unaccounted errors, ρ_{cl} is Clean Mirror Reflectance that are equal to 0.974, 0.994, 0.98, reflectivity $1/\rho_{cl}$, $(1+\varepsilon_4')/2$, 0.96, 0.935, respectively [27]. K is incident angle modifier which is equal to:

$$K = \cos(\theta) + 0.000884\theta - 0.00005369\theta^2 \quad (37)$$

Where θ is tilted angle of solar collector.

3.2.6.2. Solar Irradiation Absorption in the Absorber

$$\dot{q}_{3 \text{ SolAbs}}' = \dot{q}_{si}' \eta_{|i|} \alpha_{|i|} \tau_{env} \quad (38)$$

With

$$\eta_{|i|} = \eta_{env} \tau_{env} \quad (39)$$

Where $\eta_{|i|}$ is the effective optical efficiency at the glass pip, $\alpha_{|i|}$ is the absorber's absorptance, τ_{env} is the transmittance of the glass envelope, and η_{env} is the absorber's absorptance.

3.2.7. Heat Loss through Support Bracket

Support brackets that extend from the collector structure to the receiver support the HCEs at the collector focal line. Every HCE has a support bracket at the ends (every 4 meters of receiver length), and the current work is supported by two of these brackets. By modeling the support bracket as an infinite fin with a base temperature 10 degrees lower than the outer absorber surface temperature T_3 at the attachment point, the bracket losses may be roughly calculated. [25].

$$\dot{q}_{cond, bracket}' = \sqrt{\bar{h}_b P_b k_b A_{cs, b}} (T_{base} - T_6) / L_{HCE} \quad (40)$$

Where, in accordance with section 3.2.5.1, \bar{h}_b is the average convection coefficient of the bracket that is dependent on wind speed. P_b is the bracket's perimeter, k_b is its conduction coefficient, $A_{cs, b}$ is its minimum cross-sectional area, T_{base} is the temperature at the bracket's base, T_6 is the surrounding air temperature, and L_{HCE} is the length of the HCE. The HCE support bracket has a circumference of 0.2032 m, a cross-sectional area of $1.613e-4 \text{ m}^2$, and a conduction coefficient for plain carbon steel that is constant at 48 W/m-K.

3.3. Exergy analysis

The outcome of applying the second law of thermodynamic on PTSC is:

$$\dot{E}x_{f, in} + \dot{E}x_s = \dot{E}x_{f, out} + \dot{E}x_l + \dot{E}x_{des} \quad (41)$$

Where $\dot{E}x_{f, \in}$ is exergy input to the fluid flow, $\dot{E}x_s$ is exergy flow on entering solar radiation exergy flow on incoming solar radiation, $\dot{E}x_{f, out}$ is output exergy of the fluid flow, $\dot{E}x_l$ is the exergy loss and $\dot{E}x_{des}$ is the exergy destruction. Quantity of energy flow based on received solar radiation can be estimated by Petela-Landsberg-Press equation [28]:

$$\dot{E}x_s = \dot{Q}_s \times \eta_{PLP} = \dot{Q}_s \times \left(1 - \frac{4}{3} \times \left(\frac{T_{amb}}{T_{sun}} \right) + \frac{1}{3} \times \left(\frac{T_{amb}}{T_{sun}} \right)^4 \right) \quad (42)$$

The Petela-Landsberg-Press equation is constraint to fully concentrated solar radiation, 46200 or so, and blackbody absorbers. Since the PTSC have smaller concentration ratio and their absorber is not blackbody, so prior Equation is not valid on this condition. Eventually, following equation is proposed to estimate the amount of exergy flow that is incoming in PTSC from the sun [29].

$$\dot{E}x_s = \dot{Q}_s \times \alpha \left(1 - \frac{4}{3} \times \left(\frac{T_{amb}}{T_{sun} \times l} \right) + \frac{1}{3} \times \left(\frac{T_{amb}}{T_{sun} \times l} \right)^4 \right) \quad (43)$$

Where T_{sun} is the temperature of sun surface and supposed by 5780 (k) and l is the interaction factor and calculated by following Equation [30].

$$l = \left(\frac{f_H \times \varepsilon_H \times \alpha}{f_r \times \varepsilon_r} \right)^{0.25} \quad (44)$$

Where f_H is the view factor that takes the geometrical relation between the radiation source of the absorber of radiation, ε_H is the dilution factor that hits on a surface from a radiation source of view factor and f_r is Geometric Factor of the emitted radiation by the Absorber.

Calculating the usable exergy involves comparing the exergy of the fluid imported into and exported from the collector [31]:

$$\dot{E}x_u = \dot{E}x_{f, out} - \dot{E}x_{f, \in} - \dot{m}_f \times C_p \times T_{amb} \times \ln \left(\frac{T_{out}}{T_{in}} \right) - \dot{m}_f \times T_{amb} \times \left(\frac{\Delta P}{\rho_f \times T_f} \right) \quad (45)$$

Where ΔP is the pressure drop value.

The value of exergy loss is equal to [32]:

$$\dot{E}x_l = \dot{E}x_{l, opt} + \dot{E}x_{l, thermal} \quad (46)$$

Where $\dot{E}x_{l, opt}$ is the optical exergy loss, and $\dot{E}x_{l, thermal}$ is the thermal exergy loss, which are calculated by two previous Equations, respectively [33].

$$\dot{E}x_{l, opt} = (1 - \eta_{opt}) \times \dot{E}x_s \quad (47)$$

$$\dot{E}x_{l,thermal} = \dot{Q}_l \times \left(1 - \frac{T_{amb}}{T_r}\right) \quad (48)$$

The irreversibility that is developed in the heat transfer term is revealed by exergy destruction. This parameter specifically denotes a potential work that vanishes when thermal energy is moved from a hot to a cold resource. The extent of energy destruction is evident [34]:

$$\dot{E}x_{des} = \dot{E}x_{des,s \rightarrow r} + \dot{E}x_{des,r \rightarrow f} \quad (49)$$

In PTSCs, the exergy destruction contains two main terms; one is between the Sun and the absorber tube, and the other is between the absorber and heat transfer fluid [32].

$$\dot{E}x_{des,s \rightarrow r} = \eta_{opt} \times \dot{E}x_s - Q_{s \rightarrow r} \times \left(1 - \frac{T_{amb}}{T_r}\right) \quad (50)$$

$$\dot{E}x_{des,r \rightarrow f} = \dot{Q}_u \times \left(1 - \frac{T_{amb}}{T_r}\right) - \dot{E}x_u \quad (51)$$

Eventually, the exergy efficiency can be calculated from following Equation [34]:

$$\eta_{exergy} = \frac{\dot{E}x_u}{\dot{E}x_s} \quad (52)$$

3.4. Economic modeling

The total net present cost (NPC) of PTSC is given by following equation [35]:

$$NPC = CRF \times (C_{O\&M} + C_s) \quad (53)$$

With

$$CRF = \frac{i(1+i)^n}{(1+i)^n - 1} \quad (54)$$

Where CRF is capital recovery factor, $C_{O\&M}$ is operation and maintenance costs which is equivalent to 2% of the initial investment cost, C_s (\$) is the cost purchase, i is interest rate which is equal to 2% and n is number of years.

The heat production cost of PTSC is given by following equation [35]:

$$C_H = \frac{NPC/N}{q_u} \quad (55)$$

Where N is annual number of operation hours and q_u is useful heat transfer to the HTF.

The purchase costs of the proposed system components are presented in Table 2 [35,36].

Table 2: The estimated system components' purchasing prices

| Number | Components | Unit | Price | reference |
|--------|-----------------------------|----------|----------------------------|-----------|
| 1 | Solar collector | $\$/m^2$ | 148 | [37] |
| 2 | Heat Transfer fluid (water) | $\$/m^2$ | 4 | [37] |
| 3 | Storage tank | $\$/m^2$ | 27 | [37] |
| 4 | Pump component | \$ | $3540(\dot{W}_p^0)^{0.71}$ | [36] |

3.5. Environmental analysis

3.5.1. Energoenvironmental

Environment analysis of a system was introduced by Faizal et al. [38] according to following equation:

$$x_{co2} = y_{co2} \times \dot{Q}_u \times t_{working} \quad (56)$$

Where x_{Co2} is the released CO_2 amount at the considered time in $kg CO_2$, and y_{co2} is the CO_2 emission value associated to the reference energy system gained by the life-cycle assessment approach. Additionally, \dot{Q}_u is the generated power rate of the reference system, and $t_{working}$ is the system's working time.

The life cycle assessment, LCA, is one of the environmental assessment techniques that is now used as a common and all-purpose technique in the evaluation of the environmental impact of processes and goods. The life cycle assessment is the criterion for determining how each action will affect the environment. The third component of a sustainable assessment is completed by this parameter together with economic and technical evaluations. Along with the economic and technological effects, it is important to consider the environmental ones. This technique evaluates the environmental effects of each human activity or product, including the processes involved in its extraction, manufacture, lifetime, disposal, and recycling. Table 3 presents the comparison among different values related to carbon dioxide emission value in various systems [39]. It should be to state that the values showed in Table 3 are obtained by the LCA method.

Table 3: Different values related to carbon dioxide emission value in various systems

| System type | carbon dioxide emission amount [40] (kg CO2/kWh) | carbon dioxide emission amount [41] (kg CO2/kWh) |
|-------------|--|--|
|-------------|--|--|

| | | |
|-------------------------|---------------|-------------|
| Hydraulic | 0.0037-0.237 | 0.010-0.013 |
| Wind | 0.0097-0.1237 | 0.009-0.010 |
| Solar thermal | 0.0136-0.202 | 0.013 |
| Nuclear | 0.0242 | 0.066 |
| Biomass | 0.035-0.178 | 0.015-0.041 |
| Solar PV | 0.0534-0.250 | 0.032 |
| Gas | 0.6076 | - |
| Oil | 0.7421 | 0.778 |
| Coal | 0.9753 | 0.960-1.050 |
| Biogas | - | 0.011 |
| Natural gas | - | 0.443 |
| Geothermal | - | 0.038 |
| Fuel cell | - | 0.664 |
| Solar collector [42] | 0.00647 | |

3.5.2. Exergoenvironmental analysis

Another approach that suggested for a system's environmental assessing is exergoenvironmental (EXEN) analysis. The analysis is shown as following equation by Caliskan et al. [42]:

$$x_{\text{ex},\text{co2}} = y_{\text{co2}} \times \dot{E} x_u \times t_{\text{working}} \quad (57)$$

A system's environmental analysis is comparable to its EXEN analysis. The difference is that energy values are used in environmental analysis systems, whereas exergy values are used in EXEN analysis. Because the values derived from exergoenvironmental analysis are lower than those derived from energoenvironmental analysis, the energoenvironmental analysis is, in general, a more wary criteria.

3.6. Enviroeconomic analysis

3.6.1. Energoenviroeconomic analysis

According to following equation the enviroeconomic analysis of solar systems has been presented by Deniz et al. [43]:

$$C_{\text{CO2}} = x_{\text{CO2}} \times C_{\text{CO2}} \quad (58)$$

Where c_{co2} is the cost of carbon dioxide emissions and C_{co2} is the environmental economic parameter. The cost of CO_2 emissions generated in the pertinent system is, in fact, the parameter that was obtained. It can also be viewed as a technique for assessing how energy systems affect the environment [44]. Several techniques and strategies can be used to reduce CO_2 emissions as much as feasible in order to prevent climatic variation similar to some events, such as global warming. The carbon released cost technique with an economic perspective aims to increase the relatability of the environmental effects. This technique combines punitive and

incentive strategies to lessen the negative effects of energy systems on the environment.

Based on varied legislation, the cost of the generated carbon varies by country and ranges from 13 to 16 dollars per tonne of carbon dioxide [45]. This analysis takes into account a mean value for price changes of 14.5 (\$/ton), which is equal to 0.0145 (\$/kg) of carbon dioxide [46].

3.6.2. ExergoEnviroEconomic analysis

An analysis of a system's energy and economics is similar to its analysis of its environment and economy. The calculations in the exergoeconomic analysis are based on the exergy parameter, whereas those in the enviroeconomic analysis are based on the energy parameter. In this regard, the exergoeconomic analysis for solar energy systems is suggested using Equation [46].

The interactions between the six broad parameters that have been introduced are shown in Figure 3, together with the contributions made to each of the four quantities energy, exergy, environmental impact, and economic domain. The connection between the exergy and environmental domains widens the EXEN area, as seen in Figure 3. The ENEN domain develops as a result of interactions between the energy and environmental domains. EXENEX is produced in a similar manner through the intersection of the energy, environmental, and economic realms. The interplay between the energy, environmental, and economic realms leads to the development of ENENEC.

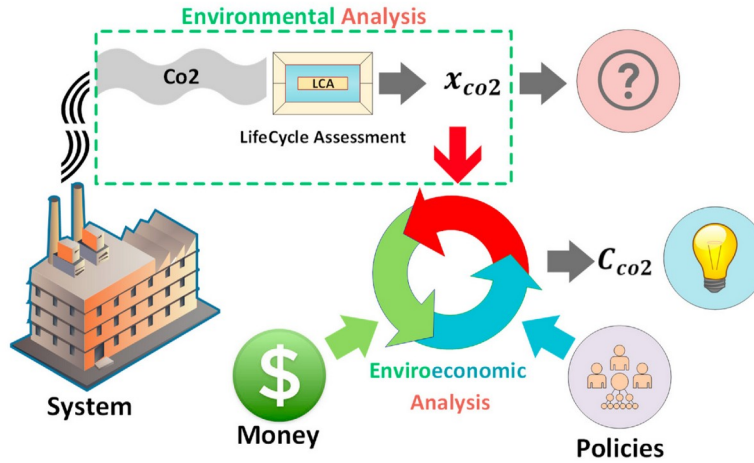


Figure 3: Detailed interaction between environment and economy

3.7. Machine Learning

A group of methods and tools known as artificial intelligence can be used to empower computers to carry out difficult jobs. The first artificial intelligence systems were created in 1950, but for a very long time there were no practical applications because computers could not process massive amounts of data. A breakthrough in artificial intelligence has

occurred since 2010 [47]. Since there have been so many advances in the field of computer science, anyone can now create their own artificial intelligence.

As it can be seen in Figure 4, neural networks are a sub-section of machine learning approaches, and Artificial Intelligence and Data Science are in common in Machine learning. Machine Learning includes, Neural Networks, Evolutionary Algorithms, Search and Reinforcement learning. This progress has brought up both new opportunities and risks. Cars can crash, patients can be wrongly diagnosed, people's privacy can be invaded, and people can be unfairly stigmatized based on their ethnicity and appearance as a result of errors made by AI algorithms. Therefore, it is crucial to inform anybody working with AI about what AI is, how it functions, and what errors can occur while utilizing artificial intelligence.

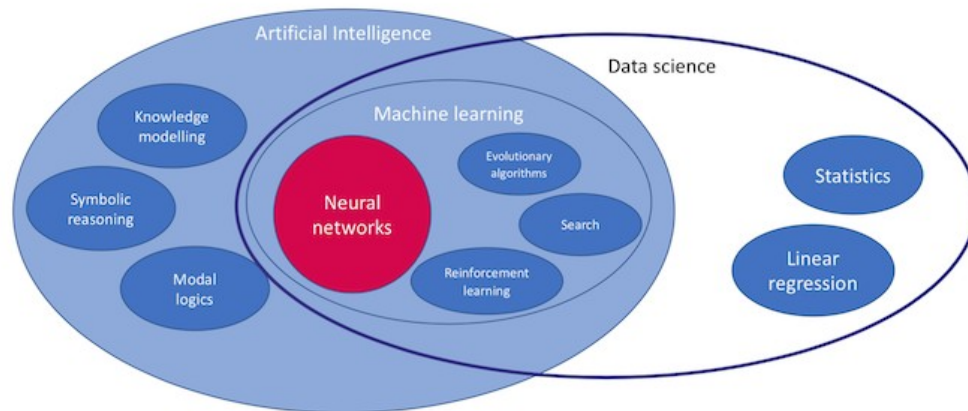


Figure 4: Relatives among, Machine Learning, Artificial Intelligence and Data Science, Neural Networks and other related fields [47]

3.8. Neural network algorithm

Artificial Neural Networks (ANN) have had a striking expansion in recent years, both in basic and applied research. This is due to the fact that ANN is a cutting-edge approach that has never been used before and can resolve challenging linear and non-linear issues for which traditional mathematics, algorithms, and methodologies have been unable to come up with an adequate and acceptable answer [48].

Machine learning algorithms known as ANNs are based on how the human brain functions, which is included several artificial neurons related to a parallel network. These networks function by connecting the inputs and outputs of the entire system using non-linear mapping techniques [49].

The fundamental structure of an ANN consists of an input layer, one or more hidden layers, and an output layer. Each neuron in the output layer

receives the information from the layer above. Each output neuron receives information from the buried layer. Each neuron in the hidden layer receives information from the input layer, whereas the input layer receives information from the experiment. The link between neurons and layers is connected with a weight value and a compensation value known as bias, allowing them to cooperate. The mathematical equation that describes how the network works is as follows:

$$n_j = \sum_{k=1}^K (IW_{s,k} P_{\dot{i}} + b_{1(s)}) \quad (59)$$

$IW_{s,k}$ are the coefficients of the connection weights between the input layer and the hidden layer, $P_{\dot{i}}$ are the input variables, and $b_{1(s)}$ is the bias by corresponding to the neuron in the hidden layer, where K is the number of input data ($k=1,2,3 \dots K$). The data is stored as a set of biases and weights for connections. Following the addition of the weighted inputs from various connections and the compensation value, a transfer function is applied to neuron J of the hidden layer:

$$a_j = F \left(\sum_{k=1}^K \square (IW_{s,k} P_{\dot{i}} + b_{1(s)}) \right) \quad (60)$$

In which Y_k experiences the same process as described by:

$$Y_k = F \left(\sum_{s=1}^S \square (L W_{l,s} a_j + b_{2(l)}) \right) \quad (61)$$

Transfer functions are used to return output for a specific range of input values in the hidden layer. The most widely used transfer functions are the tangential-sigmoidal (TANSIG) and logarithmic-sigmoidal (LOGSIG), which are determined by Transfer function using a logarithmic sigmoid:

$$F(n_j) = LOGSIG(n_j) = \frac{1}{1 + e^{-n_j}}, 0 < F(n_j) < 1 \quad (62)$$

Hyperbolic tangent sigmoid transfer function is given by:

$$F(n_j) = TANSIG(n_j) = \frac{1 - e^{-2n_j}}{1 + e^{-2n_j}} = \frac{2}{1 + e^{-2n_j}} - 1, -1 < F(n_j) < 1 \quad (63)$$

To enhance experimental data prediction in the output layer, the linear transfer function (PURELIN), which is defined as:

Linear transfer function:

$$F \left(\sum_{s=1}^S \square (L W_{l,s} a_j + b_{2(l)}) \right) \quad \dot{i} \quad PURELIN \left(\sum_{s=1}^S \square (L W_{l,s} a_j + b_{2(l)}) \right) \quad (64)$$

It is important to note that before training the neural network, standardizing each input variable is a valuable tool. Interval operating of

non-linear transfer functions is the first step in training for increased efficiency. The input normalization technique typically scales the data using a linear mapping known as the min max scale.

The following equation is utilized to standardize the input variables [50]:

$$p_{i,N} = \frac{(P_i - P_{min})}{P_{max} - P_{min}} (Y_{max} - Y_{min}) + Y_{min} \quad (65)$$

Where $p_{i,N}$ represents the normalized variable, P_i represents the variable's actual value prior to normalization, P_{max} and P_{min} express the variable's maximum and minimum values prior to normalization, and Y_{max} , Y_{min} state the variable's maximum and minimum values following normalization.

To evaluate the effectiveness of the ANN model, experimental data were compared to simulated data using statistical analysis. Three often utilized test parameters are the Root Mean Square Error (RMSE), Mean Absolute Percentage Error (MAPE), and Coefficient of Determination (R^2) [51]. Ideal models are those with (R^2) values that are near to 1, as well as MAPE and RMSE values that are close to 0. To verify the linearity and accuracy of the model, the intercept-slope test was also carried out with slope = 1 and intercept = 0.

$$RMSE = \sqrt{\frac{\sum_{i=1}^n (X_{out, exp(i)} - X_{out, \sim(i)})^2}{n}} \quad (66)$$

$$MAPE = \frac{\sum_{i=1}^n \left| \frac{X_{out, exp(i)} - X_{outs, sim(i)}}{X_{out, exp(i)}} \right|}{n} \times 100(\%) \quad (67)$$

$$R^2 = 1 - \frac{\sum_{i=1}^n (X_{out, exp(i)} - X_{out, \sim(i)})^2}{\sum_{i=1}^n \hat{\epsilon}_i^2} \quad (68)$$

where $\hat{X}_{out, exp} = \frac{1}{n} \sum_{i=1}^n X_{out, exp(i)}$, $X_{out, \sim(i)}$ is the gained output value by ANN, and $X_{out, exp(i)}$ is the experimental output value.

The matrix of weights was used in a sensitivity analysis after the ANN model had been trained to determine the relative contribution of each input variable to the output variable and to determine bias. According to the split of the connection weights, Garson [52] proposed the following equation:

$$I_j = \frac{\sum_{m=1}^{N_h} \left(\left(\frac{|w_{jm}^{ih}|}{\sum_{k=1}^{N_i} |w_{km}^{ih}|} \right) |w_{mn}^{ho}| \right)}{\sum_{k=1}^{N_i} \left(\left(\sum_{m=1}^{N_h} \left(\frac{|w_{km}^{ih}|}{\sum_{k=1}^{N_i} |w_{km}^{ih}|} \right) \right) |w_{mn}^{ho}| \right)} \quad (69)$$

Where I_j represents the relative weight of the j^{th} input variable on the output variable, and N_i and N_h represent the number of neurons in the hidden and input layers, respectively. The input, hidden, and output layers are indicated by the superscripts I, h , and o . Input, hidden, and output neurons are identified by the subscripts k, m , and n , respectively.

3.9. Proposed Machine Learning Approach

Solving a striking number of equations in engineering requires high time, energy, cost, and bulk of calculation because there are usually multiple equations with multiple unknowns, multiple physics, complex physics, non-linear equations, or coupled equations. Sometimes, solving equations and extracting solutions to respond quickly and satisfy objectives is an essential requirement. The approach with these hindrances is not only executable with elevated hardware computers, but also difficult for custom personal computers. Thus, it is being tried to solve these barriers in a subtly affordable way. In this respect, applying a confirmed and accurate machine learning model could be troubleshooting and redeeming. Figure 5 illustrates the applied approach as a comprehensive depiction, including procedure selection, pre-processing of data, post-processing of data, training, desired circumstances, and achievements.

In addition, applying an appropriate data scale could have a substantial impact on the precision of the model, stability, performance, and time period of training. The examples in a training dataset help the models learn how to map inputs to outputs. In order to estimates of error on the training

dataset, an optimization algorithm updates the machine learning model's weights, which are initially initialized to small random values.

The bulk of the inputs and outputs which utilized to train the model is a crucial consideration due to the modest weights used in the applied model and the utilization of error between predictions and expected values. Unscaled target variables on regression issues could lead to exploding gradients that cause the training process to collapse¹, but unscaled input variables might cause a delayed or unstable learning process.

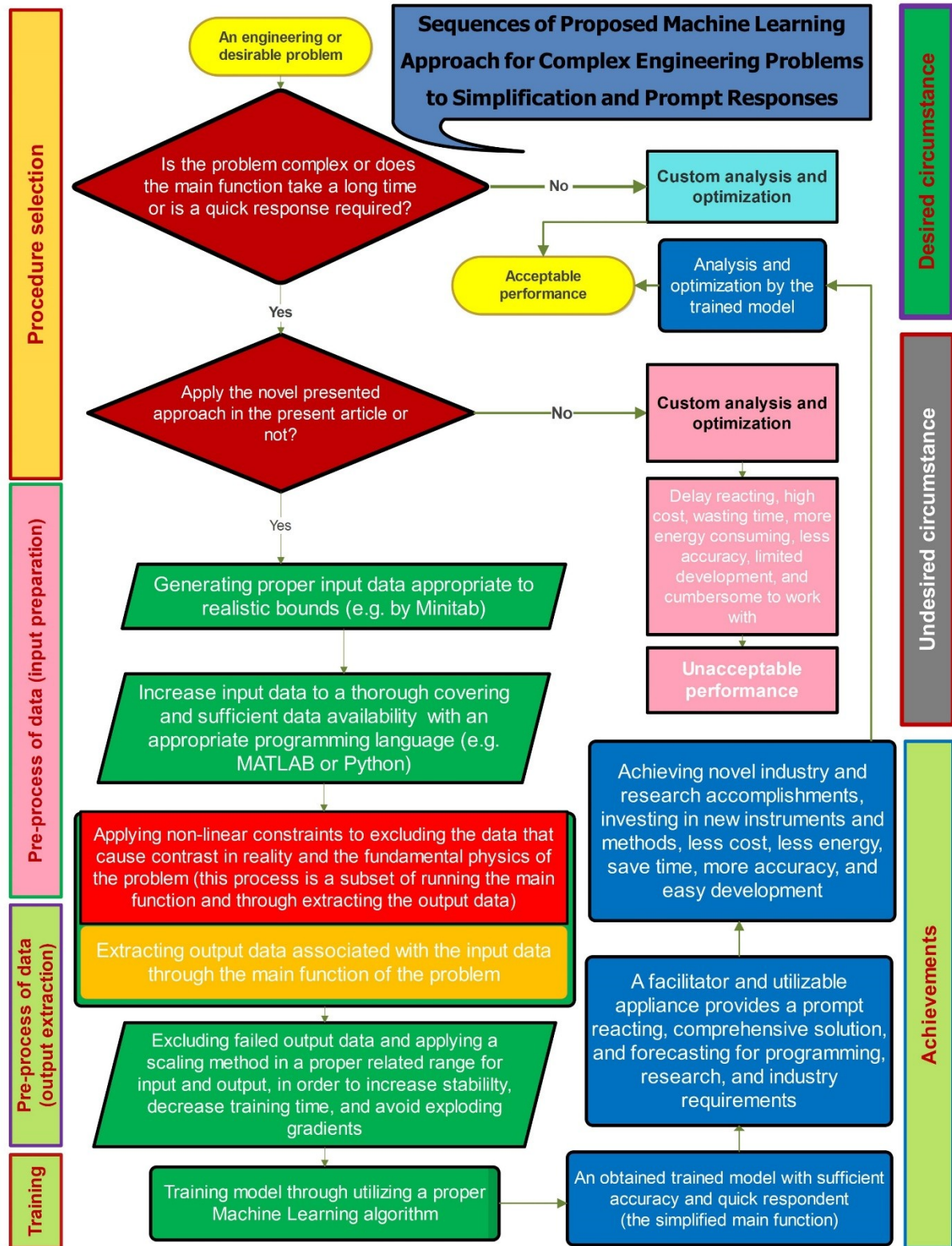


Figure 5: Sequences of proposed Machine Learning approach for complex engineering problems to simplification and prompt response

4. Results and discussion

4.1. Model description, PTSC specification and climate condition

The illustrated system in Figure 1 have been modeled based the presented Machine Learning approach and optimized for Tehran city, capital of Iran, which located at longitude $+52.5^\circ$ and latitude $+35.7^\circ$ [53].

Table 4 presents the average climate condition in Tehran, such as average air temperature, wind velocity, DNI, average monthly hours of sunshine and average monthly solar incidence angle. For this system to be applicable along the days of the year, average data considered for this optimization.

Table 6 shows the specifications of PTSC, and The heat transfer constants and coefficients for each annulus gas are listed in Table 7, which are studied in this article. One main code is generated in MATLAB software to calculate the parameters of the PTSC, one code is prepared for the GA algorithm, and one code is written to considering non-linear constraints of the PTSC optimization.

4.2. Validation of model

The modeling and generated codes in this work are validated with Ref [54]. Climate circumstances examined in reference [54], as well as the PTSC specification, are regarded as input data. Figure 3.2, and Table 3.3 of that reference are considered. In those tables and figures outlet temperature of HTF, the difference between the average HTF and the ambient temperature (T_{diffAir}), useful heat transfer and energy efficiency are calculated for the mean values along the year. Table 5 shows how the outcomes of this modeling were compared to reference experimental data [54].

Table 4: The average climate condition in Tehran including Air temperature, wind velocity, DNI, average Monthly Hours of Sunshine, and average monthly solar incidence optimum angle

| month s | Value | | | | |
|------------|--|-----------------------------------|--------------------|--|---|
| | Air temperat ure ($^\circ C$) | Wind velocit y (m/s) | DNI (KWh/n) | Average Monthly Hours of Sunshine (hr) | average monthly solar incidence optimum angle ($^\circ$) |
| Jan | 5.8 | 2.6 | 2.7 | 7.2 | 63.1 |

| | | | | | |
|----------------|-------|------|------|------|------|
| Feb | 8.4 | 2.6 | 3.5 | 7 | 53.8 |
| Mar | 16.9 | 4.2 | 4.5 | 9.3 | 38.4 |
| Apr | 16.7 | 3.2 | 5.5 | 11.2 | 17.5 |
| May | 21.3 | 3.6 | 6.4 | 11.8 | 0.1 |
| Jun | 29.1 | 3 | 7.3 | 12.2 | -8.1 |
| Jul | 33.9 | 2.9 | 7.0 | 12 | -6.1 |
| Aug | 31.6 | 2.9 | 6.5 | 12 | 7.5 |
| Sep | 26.9 | 2.9 | 5.6 | 11.6 | 26.5 |
| Oct | 19.1 | 2.8 | 4.0 | 7.5 | 43.5 |
| Nov | 10.9 | 2.2 | 2.9 | 7.2 | 54.0 |
| Dec | 8.9 | 1.7 | 2.4 | 7.2 | 57.1 |
| Annual average | 19.13 | 2.88 | 4.86 | 9.68 | 28.9 |

Table 5: Comparison of presented modeling outcomes with experimental data [54]

| Parameter | Reference [54] | Present model | Error (%) |
|---------------------------|----------------|---------------|-----------|
| $T_{outlet} (^{\circ}C)$ | 124 | 123.7 | 0.2 |
| $T_{diffAir} (^{\circ}C)$ | 91.9 | 91.6 | 0.3 |
| Heat gain (w/m) | 3402 | 3236 | 4.8 |
| Energy efficiency (%) | 72.5 | 71.85 | 0.8 |

The maximum error of the results is 4.8 % which is due to determine the variation in heat loss between theoretical and experimental states.

Table 6: The specifications of PTSC [54]

| Number | Parameter | Unit | Value |
|--------|--------------------------|--------|-------|
| 1 | $\alpha_{absorber}$ | $-i$ | 0.955 |
| 2 | $\varepsilon_{absorber}$ | $-i$ | 0.15 |
| 3 | k_{glass} | W/mK | 1.04 |
| 4 | ε_{glass} | $-i$ | 0.86 |
| 5 | τ_{glass} | $-i$ | 0.965 |
| 6 | α_{glass} | $-i$ | 0.02 |
| 7 | Mirror reflectively | $-i$ | 0.935 |

Table 7: Heat transfer coefficients and constants for each annulus gas

| Annulus Gas | k_{std} [$W/m-K$] | b [-] | λ [cm] | γ [-] | δ [cm] |
|-------------|--------------------------|---------|-----------------------|--------------|--------------------|
| Air | 0.02551 | 1.571 | 88.67 | 1.39 | 3.53×10^8 |
| Hydrogen | 0.1769 | 1.581 | 191.8 | 1.398 | 2.4×10^8 |
| Argon | 0.01777 | 1.886 | 76.51 | 1.677 | 3.8×10^8 |

4.3. Application of proposed Machine Learning Approach

In the present article, the comprehensive proposed procedure is implemented for a complex problem that deals with energy, environmental, and economic issues and their consequences. This approach is defined and performed with all the

details and is extendable to the other complex problems in engineering, including heat transfer, thermodynamics, fluid mechanics, and any other disciplines of science which are collided with the mentioned obstacles or any other complexities. Dealing with non-linear multiple equations and multiple unknowns, a few times and in different places, is one of the complexities of this article's problem. Solving non-linear five equations with five unknowns for extracting temperature distributions in various zones causes to consume high time, energy and amount of calculation. For this case study, the period of time needed for each main function is equal to 8 seconds, and optimization period time is estimated to:

$$250(\text{generations}) \times 200(\text{populations}) \times 8(\text{runtime of the main function}) = 111.1 \text{ hr}$$

These periods are too long and energy-consuming. Additionally, they do not provide acceptable time solutions to theoretical problems, and do not satisfy quick responses in industrial applications. Therefore, an attempt to simplify the issues and overcome the obstacles is an essential requirement.

The primary standard input data was generated with Minitab by creating a central composite full of response surface design. After that, the number of continuous and categorical factors was defined as seven and three, respectively. Then, related upper and lower bounds were assigned. After creating the adjustment options, 6912 base runs were generated as input data. Then, a MATLAB code is generated to increase the input data to provide sufficient data. The input data was increased to 173631 data. Next, the main function code of the system ran for the number of data. While running the main function, the essential point is to apply the non-linear constraints to avoid non-physical data. There is some failed output data as a result of satisfying the non-linear constraint. After skimming the failed data, the bulk of utilizable data remained for 45835.

The following content includes training a proper and accurate machine learning model to achieve immediate response, consuming less time process, less calculation requirements, and energy due to treating the problem conveniently. In addition, the effect of various parameters of training is discussed.

For training of the model of PTSC, several inputs and outputs are considered. Outputs include energy efficiency (%), exergy efficiency (%), and heat cost (\$/kwh). The heat cost function includes the cost function (\$) and useful heat gain (W), which is related to energy efficiency. According to the changing of seven continuous variable values with related bounds in Table 8 and three categorical variables in Table 9, the target is to provide an accurate model between inputs and outputs. It should be noted that some of the outputs are not independent, and they could be calculated from the other independent outputs. It is possible to consider more outputs to elevate the accuracy of prediction or based on desired parameters by presented tips in methodology section. The investigated inputs and output functions are presented in Table 10. In addition, the related non-linear

constraints are so vital to exact and realistic prediction while training. The non-linear constraints are presented in Table 11.

Table 8: The variation of seven continuous variable values with related bounds

| No. | Variable | Dim. | Lower bound | Upper bound |
|-----|-----------------------------|-------------|--|-------------|
| 1 | $D_{\text{inner,absorber}}$ | m | 0.01 | 0.08 |
| 2 | $R_3 - R_4$ | m | 0.005 | 0.05 |
| 3 | L | m | 2 | 100 |
| 4 | W | m | 1 | 6 |
| 5 | \dot{m} | kg/s | 0.0001 | 12 |
| 6 | P_{annulus} | pa | 0 | 88223 |
| 7 | $T_{\textcolor{red}{i}}$ | $^{\circ}C$ | 25 | 80 |
| | $D_{\text{outer absorber}}$ | m | $D_{\text{outer,absorber}} = D_{\text{inner,absorber}} + \textcolor{red}{i}$ | |
| | | | 0.003 | |
| | $D_{\text{outer,glass}}$ | m | $D_{\text{outer,glass}} = D_{\text{inner glass}} + 0.003$ | |

Table 9: The three categorical variables

| | | | | | | Variable |
|--------------|--------------|----------------|-----------------------------|---------------|--------------|------------------------|
| Therminol 72 | Syltherm 800 | Therminol TD12 | Water | Therminol VP1 | Therminol 66 | Heat transfer fluid |
| | | | Aluminum, 2024, Temper-T351 | Copper | 321H | Absorber tube material |

| | Argon | Hydroge n | Air | Annulus Gas |
|--|-------|--------------|-----|----------------|
|--|-------|--------------|-----|----------------|

Table 10: Investigated inputs and outputs for training

| | Sign | Dim. | Description |
|------------------|---------------------------------|-------------|--|
| Design variables | $D_{\text{inner,absorber}}$ | m | Inner diameter of absorber tube |
| | $R_4 - R_3$ | m | Distance between absorber and envelope |
| | \dot{m} | kg/s | Mass flow rate |
| | T_{in} | $^{\circ}C$ | Input fluid temperature |
| | L | m | Collector length |
| | W | m | Collector aperture width |
| | P_{annulus} | pa | Pressure between absorber and envelope |
| | X_{absorber} | — | Absorber tube material |
| | X_{HTF} | — | Heat transfer fluid type |
| | X_{annulus} | — | Annulus gas type |
| Outputs | $First = \eta_{\text{energy}}$ | % | energy efficiency |
| | $Second = \eta_{\text{exergy}}$ | % | exergy efficiency |
| | $Third = C_H$ | $\$/kWh$ | heat production cost |

Table 11: Applied non-linear constraints for main function for training at the same time

| Non-linear constraints | Acceptable bound |
|------------------------|-----------------------|
| HTF velocity limit | Velocity $\leq 3 m/s$ |

HTF temperature

$$T_{HTF} \wedge T_2 \leq T_{sat}$$

HTF pressure

$$P_{HTF} \geq P_{sat}$$

Exergy efficiency

$$\eta_{exergy} \geq 0$$

Figure 6 depicts the trend of training by training data, validation data, test data and the best point for each epoch. As it is shown, Mean Squared Error (MSE) or Residual Sum of Squared (RSS) is decreasing, and the best validation point is at epoch 97 with performance of 2.7263×10^{-7} .

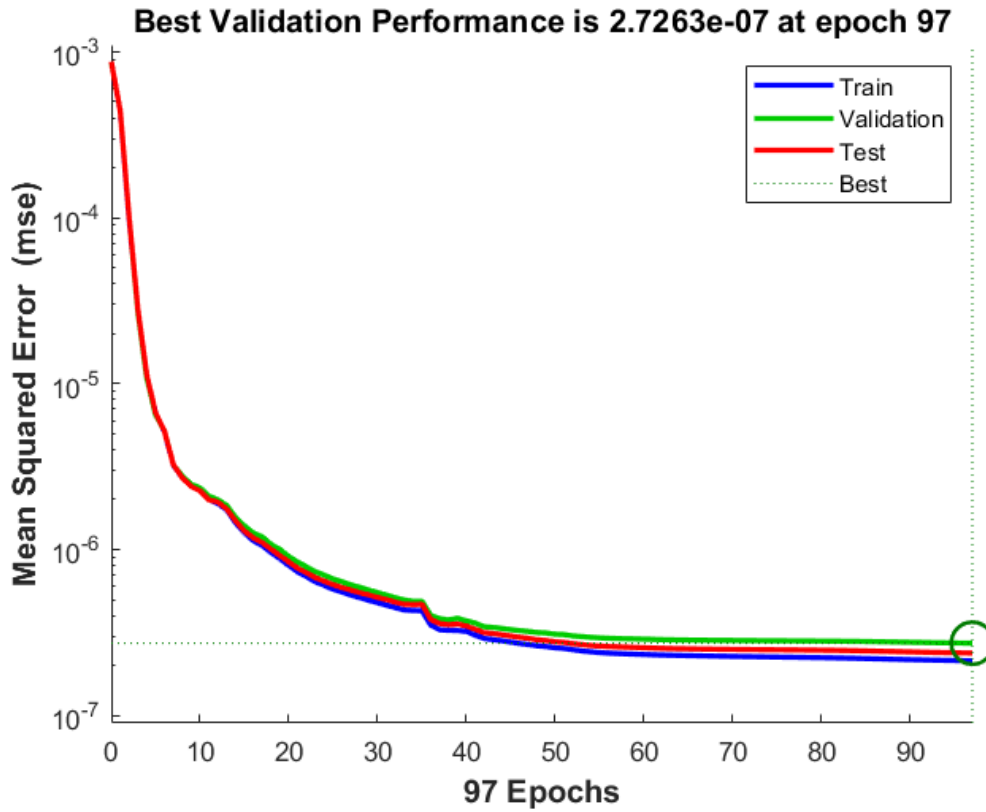


Figure 6: The variation of Mean Squared Error by Epochs with Training, validation, test data

Figure 7 illustrates the Error histogram around zero error line for instances with 20 Bins for training data, validation data and test data. The error, which is equals to targets minus outputs, is distributed between an acceptable area, which is between 0.001717 and -0.0017 .

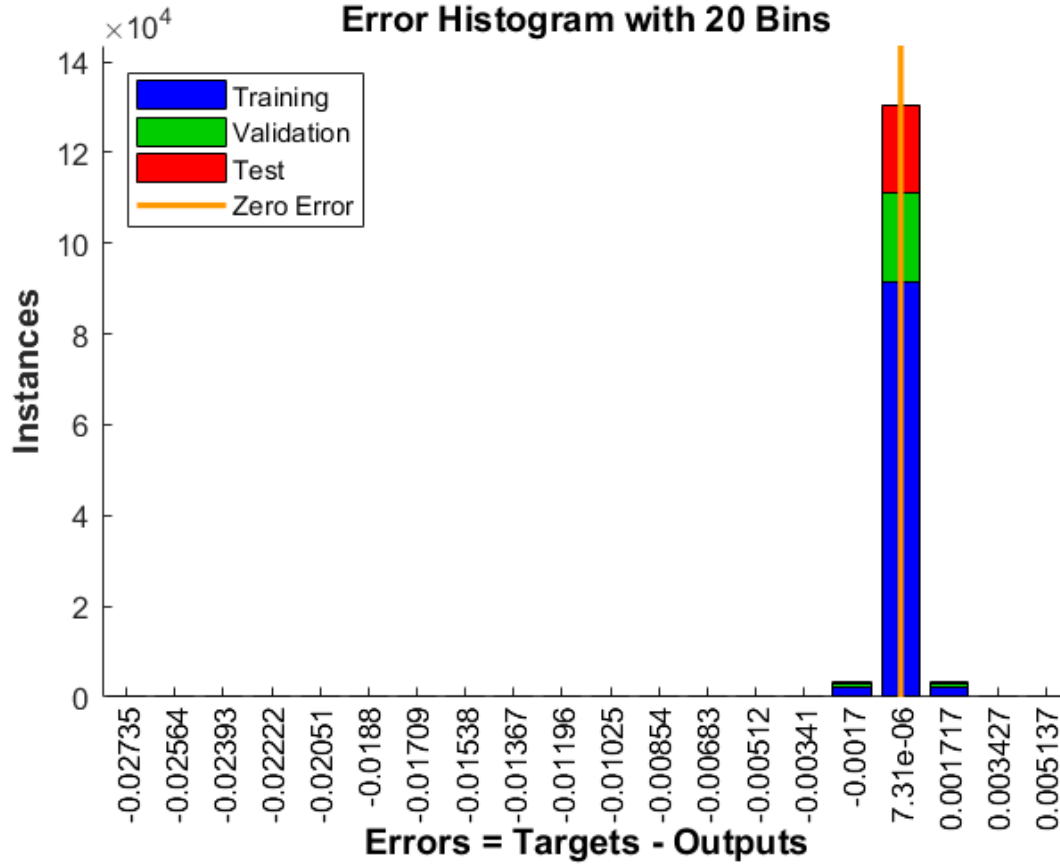


Figure 7: The Error histogram around zero error line for instances

Figure 8 shows the regression results for training data, validation data, test data and all of them in a comprehensive depiction. Outcomes confirm that an ideal regression is resulted, which the regression number is equals to 0.9999 for test data. In addition to utilize various procedures to increase accuracy, this precision is obtained from two main reason, including scaling the input and output data to an appropriate range and applying non-linear constants to ensure being physical meaningful data. The scaling data avoids generating large weight values from training model. Large weight values are frequently indicative of an unstable model, which may exhibit poor learning performance and sensitivity to input values, leading to a larger generalization error.

Assessing the results under scrutiny emerges the lack of data for regression for area that non-linear constraints banned producing data. Thus, there are no data in this vicinity, because this data is in contrary to reality and the fundamental physics of the problem. Following this approach is a substantial step to avoid misdirection, inaccurate machine learning training and generating unrealistic outputs from trained model.

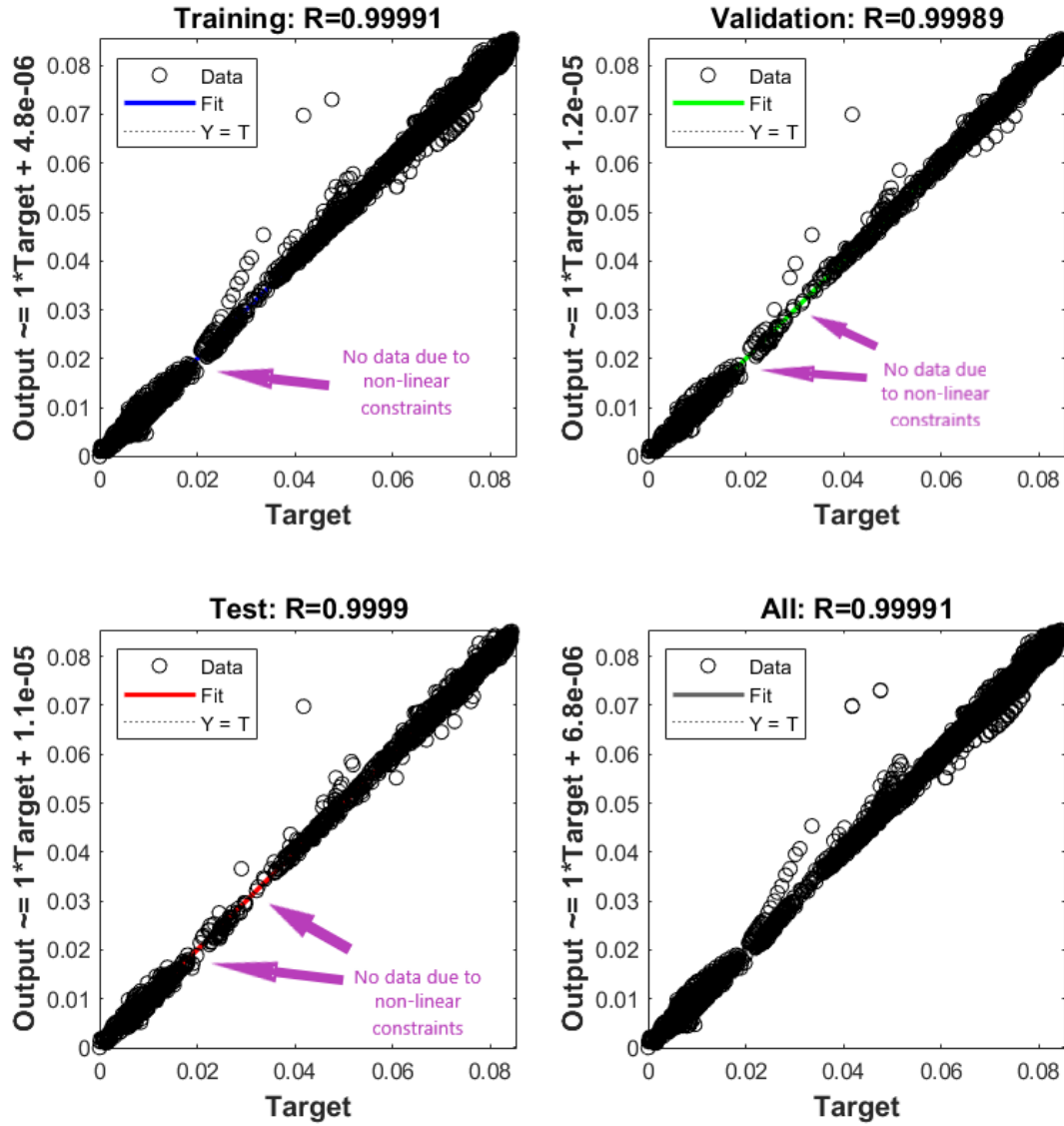


Figure 8: The Regression results for training data, validation data, test data

4.4. Optimization of PTSC

In the wake of providing an accurate proper machine learning model, executing optimization for the prior complex problem, is simple, quick and convenient for various decision variables to optimization and analysis of desired objectives.

For optimization of PTSC with GA algorithm, by trained model, two objective functions are evaluated: exergy efficiency (%) and heat cost

(\$/kwh). The heat cost function is included cost function (\$) and useful heat gain (W) which is related to energy efficiency. According to the changing of seven continuous variable values with related bounds in Table 12 and three categorical variables in Table 13, the goal is to maximize energy efficiency and reduce the cost of providing heat. Table 14 presents the variables and objective functions that were examined.

Table 12: Lower bounds and upper bounds of seven continuous variable values for optimization

| Number | Variable | Dim. | Lower bound | Upper bound |
|--------|-----------------------------|-------------|--|-------------|
| 1 | $D_{\text{inner,absorber}}$ | m | 0.01 | 0.08 |
| 2 | $R_3 - R_4$ | m | 0.005 | 0.05 |
| 3 | L | m | 2 | 4 |
| 4 | W | m | 1 | 3 |
| 5 | \dot{m} | kg/s | 0.0001 | 12 |
| 6 | P_{annulus} | pa | 0 | 88223 |
| 7 | $T_{\textcolor{red}{i}}$ | $^{\circ}C$ | 25 | 80 |
| | $D_{\text{outer absorber}}$ | m | $D_{\text{outer,absorber}} = D_{\text{inner,absorber}} + \textcolor{red}{i}$ | |
| | | | 0.003 | |
| | $D_{\text{outer,glass}}$ | m | $D_{\text{outer,glass}} = D_{\text{inner glass}} + 0.003$ | |

Table 13: categorical variables for optimization

| | | | | | | Variable |
|--------------|--------------|----------------|-----------------|---------------|--------------|---------------------|
| Therminol 72 | Syltherm 800 | Therminol TD12 | Water | Therminol VP1 | Therminol 66 | Heat transfer fluid |
| | | | Aluminum, 2024, | Copper | 321H | Absorber tube |

| | | | | |
|--|-----------------|--------------|-----|----------------|
| | Temper- T351 | | | material |
| | Argon | Hydroge n | Air | Annulus Gas |

Table 14: Determined variables and objective functions for optimization

| | Sign | Dimensi on | Description |
|---------------------|-------------------------------------|---------------|--|
| Design variables | $D_{\text{inner,absorber}}$ | m | Inner diameter of absorber tube |
| | $R_4 - R_3$ | m | Distance between absorber and envelope |
| | \dot{m} | kg/s | Mass flow rate |
| | T_i | $^{\circ}C$ | Input fluid temperature |
| | L | m | Collector length |
| | W | m | Collector aperture width |
| | P_{annulus} | pa | Pressure between absorber and envelope |
| | X_{absorber} | — | Absorber tube material |
| | X_{HTF} | — | Heat transfer fluid type |
| | X_{annulus} | — | Annulus gas type |
| Objective fcn. | $Obj.1^{st} = \eta_{\text{exergy}}$ | % | exergy efficiency |
| | $Obj.2^{nd} = C_H$ | $\$/kWh$ | heat production cost |

The main parameters of Genetic algorithm solver are presented in Table 15. Furthermore, the prior applied non-linear constraints should be applied

again for optimization as presented in Table 12. One of the benefits of applying proposed machine learning approach is to decrease optimization process time which is shorted to a logical and affordable range and descended to 1143 times less.

Table 15: Main defined parameters of Genetic algorithm solver

| Parameters | Multi objective Genetic Algorithm |
|-----------------------|---|
| Decision variables | 9 |
| Size of population | 200 |
| Fraction of crossover | 0.65 |
| Mutation function | adaptfeasible |
| Crossover function | intermediate |
| Selection function | tournament |
| Function tolerance | 10^{-4} |
| Number of generation | 250 |
| Max stall generations | 40 |
| Running time | $250 \times 200 \times 0.007$ (second)=5.8 mins |

Table 16: Non-linear constraints for optimization

| Non-linear constraints | Bounds |
|------------------------|--------|
|------------------------|--------|

| | |
|--------------------|-----------------------------------|
| HTF velocity limit | Velocity $\leq 3 \text{ m/s}$ |
| HTF temperature | $T_{HTF} \wedge T_2 \leq T_{sat}$ |
| HTF pressure | $P_{HTF} \geq P_{sat}$ |
| Exergy efficiency | $\eta_{\text{exergy}} \geq 0$ |

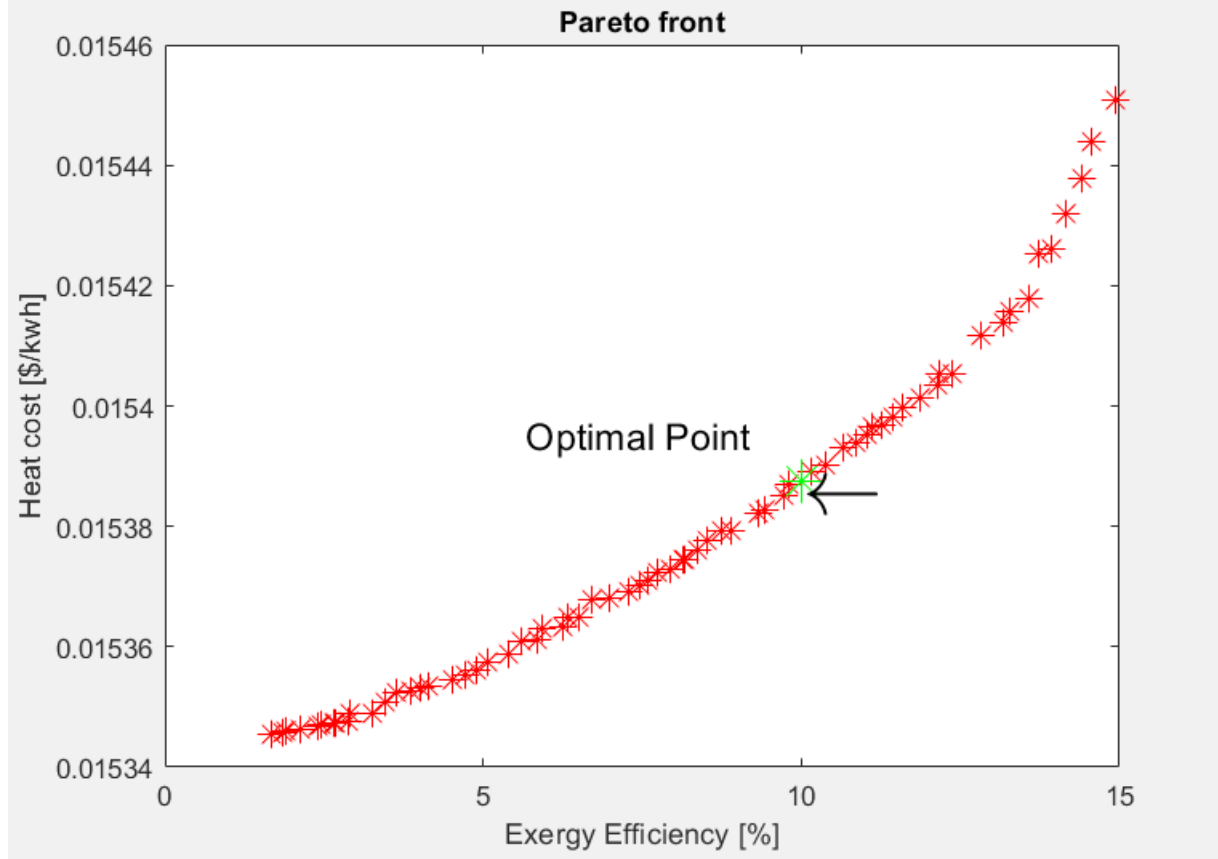


Figure 9: Pareto front of two objective functions derived from the trained model

Figure 9 illustrates the Pareto front of these two objective functions derived from the trained model. The Pareto front depicts that the exergy efficiency is ascending by increasing the heat cost function. In view of the fact that by increasing the exergy efficiency the energy efficiency is descending which cause to increase the cost function. There is an ideal point in Pareto front that never be accessible. The optimum point is obtained to the closest of the ideal point. At this point the heat cost function is equal to 0.015387 (\$/kWh) and the exergy efficiency is equal to 10.01 (%).

Investigation of aperture length and width disclosed that increasing the aperture length and width cause to increasing the exergy and energy efficiency. The cause of following content is extracting analysis of a

household PTSC from a comprehensive trained model. Nevertheless, it is logical to select the aperture dimensions according to available commercial dimensions and constructability, so dimensions are selected to 2.44 (m) and 2.29 (m) for the length and width, respectively. The concluded continuous and categorical variables are presented in Table 17. In addition, Table 18 depicts related key parameters from analysis.

Figure 10 depicts the variation of temperatures of HTF and tubes along the aperture length. The inner and outer temperatures of tubes is very close together, so in order to obvious illustration, it is showed just one of them. The outside surface of the receiver has the highest temperature, and the outer surface of the glass envelope has the lowest temperature.

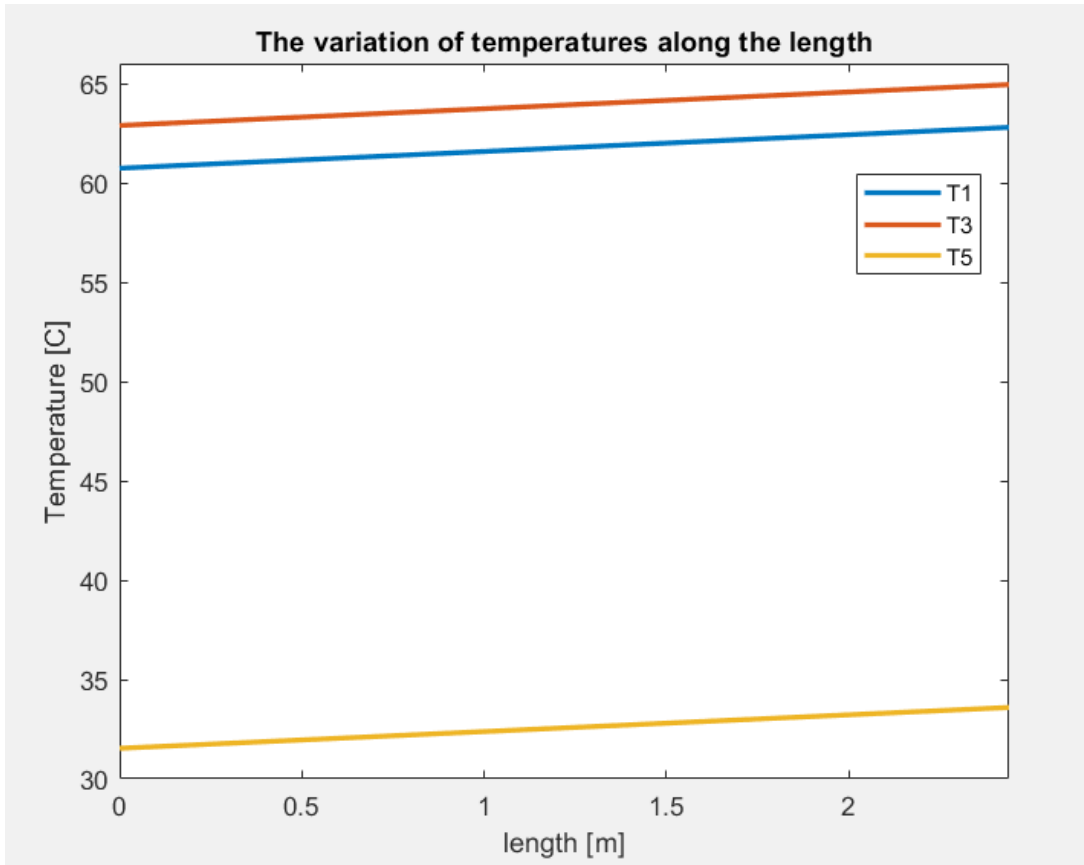


Figure 10: The variation of temperatures along the length

Table 17: Concluded continuous variables from optimization of the trained model

| N o. | Variabl e | Uni t | Values |
|---------|--------------|----------|--------|
| 1 | $D2$ | m | 0.014 |

| | | | |
|----|----------------|-------------|---------|
| 2 | $R_4 - R_3$ | m | 0.0074 |
| 3 | L | m | 2.44 |
| 4 | W | m | 2.29 |
| 5 | \dot{m} | kg/s | 0.31214 |
| 6 | T_c | $^{\circ}C$ | 60.7 |
| 7 | $P_{annulus}$ | pa | 0 |
| 8 | X_{HTF} | - | Water |
| 9 | $X_{absorber}$ | - | Copper |
| 10 | $X_{annulus}$ | - | Argon |

Table 18: Other related key parameter that outcomes from analysis

| Number | Variable | Unit | Values |
|--------|--------------------|-------------|--------|
| 1 | T_{out} | $^{\circ}C$ | 62.79 |
| 2 | q_u | w | 2685 |
| 3 | Energy efficiency | % | 74.33 |
| 4 | Exergy efficiency | % | 10.01 |
| 5 | Exergy destruction | w | 3026 |
| 6 | ΔP | Pa | 7313 |
| 7 | \Re_{D2} | - | 62365 |
| 8 | Velocity | m/s | 2.053 |

| | | | |
|---|-------|----------|----------|
| 9 | C_H | $\$/kWh$ | 0.015387 |
|---|-------|----------|----------|

4.5. variation calculation and sensitivity analysis

Figure 11 illustrates the variation of energy efficiency, exergy efficiency, heat cost, energy CO_2 emission cost and exergy CO_2 emission cost by absorber inner diameter. By increasing the absorber inner diameter from 0.01 cm to 0.08 cm, the heat cost increases. The exergy efficiency and energy efficiency are descending except at very small diameters. Due to high pressure drop and related increasing pump work, both efficiencies are decreasing at tiny diameters. By increasing the diameter, the efficiencies are declining due to decreasing in Nusselt number and convection coefficient that causes to decrease heat gain and increase exergy destruction.

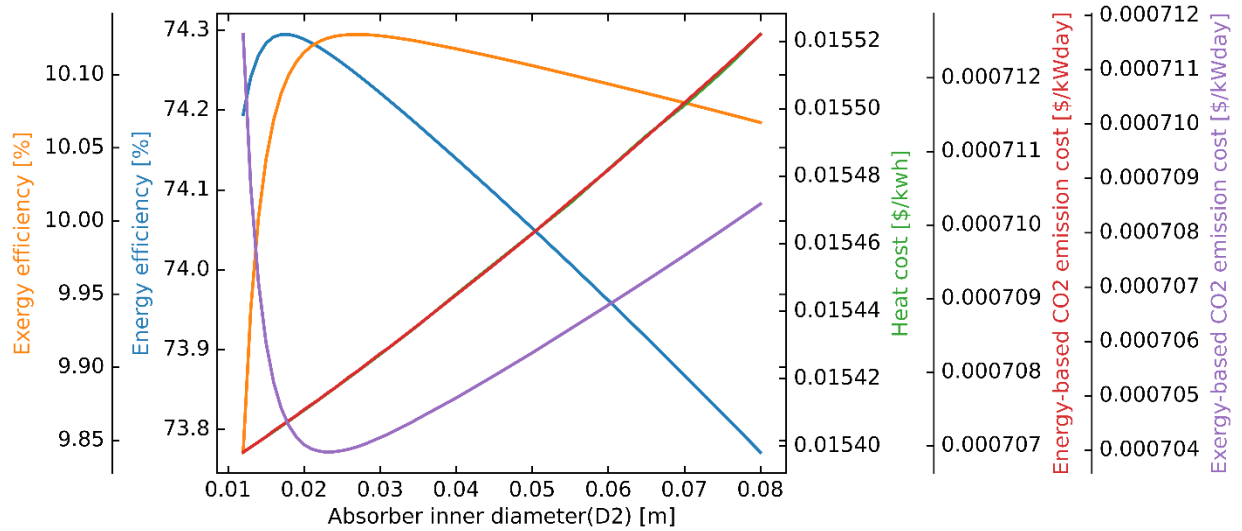


Figure 11: The variation of energy efficiency, exergy efficiency, heat cost, energy-based CO_2 emission cost and exergy-based CO_2 emission cost by absorber inner diameter

Figure 12 illustrates the variation of energy efficiency, exergy efficiency, heat cost, energy-based CO_2 emission cost and exergy-based CO_2 emission cost by distance between absorber tube and glass envelope. By increasing the distance from 0.5 cm to 5 cm, the efficiencies are descending due to declining convection heat transfer coefficient at annulus space. The energy-

based CO_2 emission cost and exergy-based CO_2 emission cost are shown as a function of prior parameters.

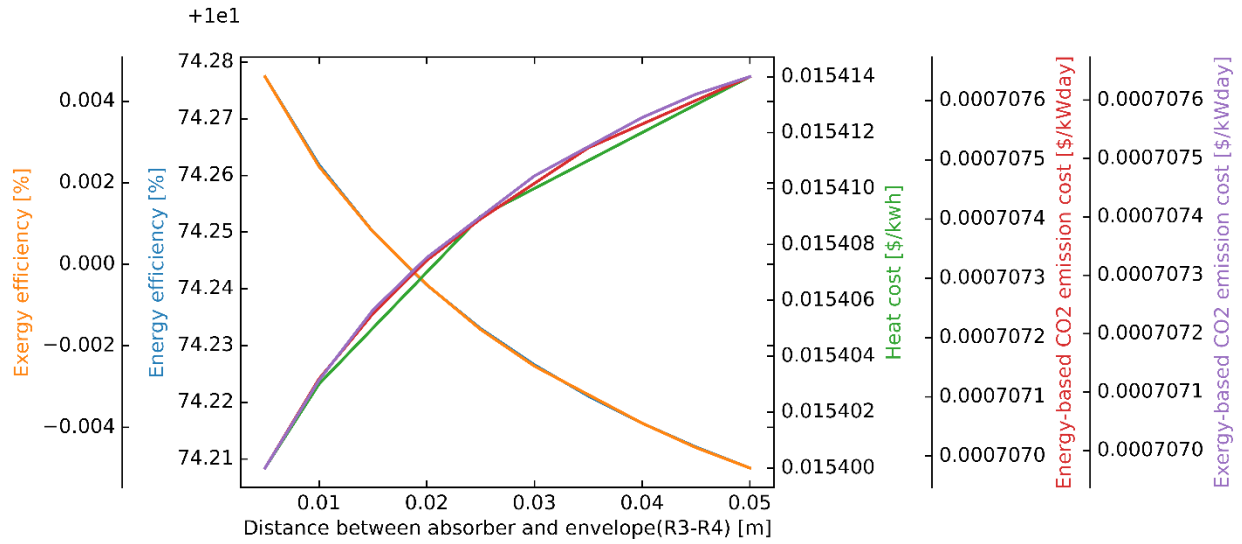


Figure 12: The variation of energy efficiency, exergy efficiency, heat cost, energy-based carbon dioxide emission cost and exergy-based carbon dioxide emission cost by distance between absorber tube and glass envelope

Figure 13 depicts the variety of energy efficiency, exergy efficiency, heat cost, energy-based CO_2 emission cost and exergy-based CO_2 emission cost by mass flow rate. By ascending mass flow rate, heat gain and destruction terms are ascending and the variation of destruction is greater than heat gain term, so the exergy efficiency is decreasing. Ascending the mass flow rate causes to increase the heat gain due to reach greater heat transfer coefficient, so the heat cost function is ascending. At this analysis, the energy efficiency is influenced by two primary parameters, the pressure drop and heat transfer coefficient. By increasing the mass flow rate both of them are increasing, but at low mass flow rates the convection heat transfer coefficient is dominant. Nevertheless, the energy efficiency is first ascending and then is descending. The energy-based CO_2 emission cost and exergy-based CO_2 emission cost are shown as a function of prior presented parameters.

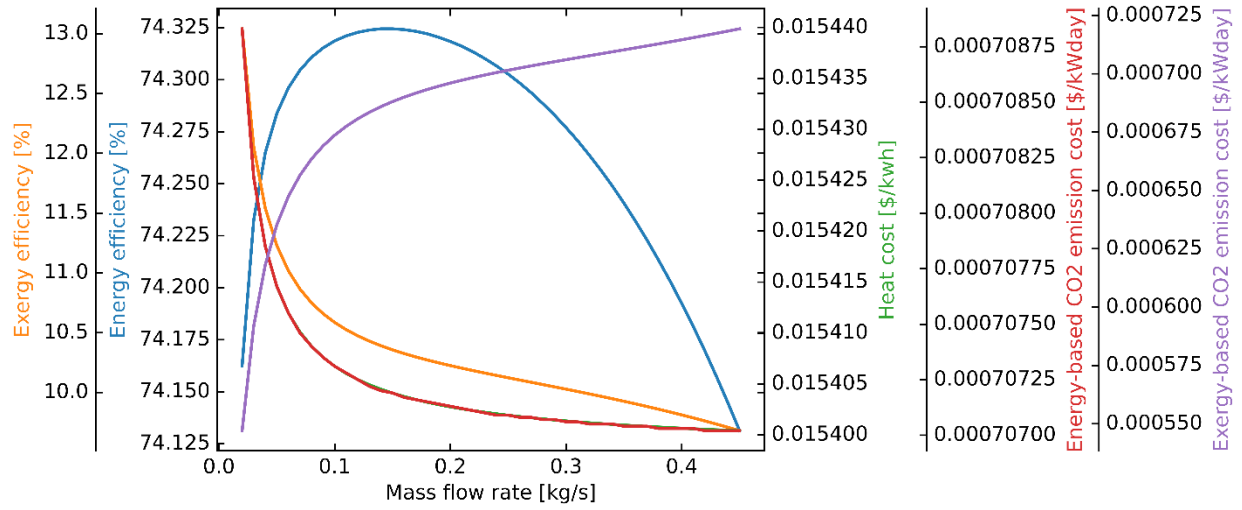


Figure 13: The variety of energy efficiency, exergy efficiency, heat cost, energy-based carbon dioxide emission cost and exergy-based carbon dioxide emission cost by mass flow rate

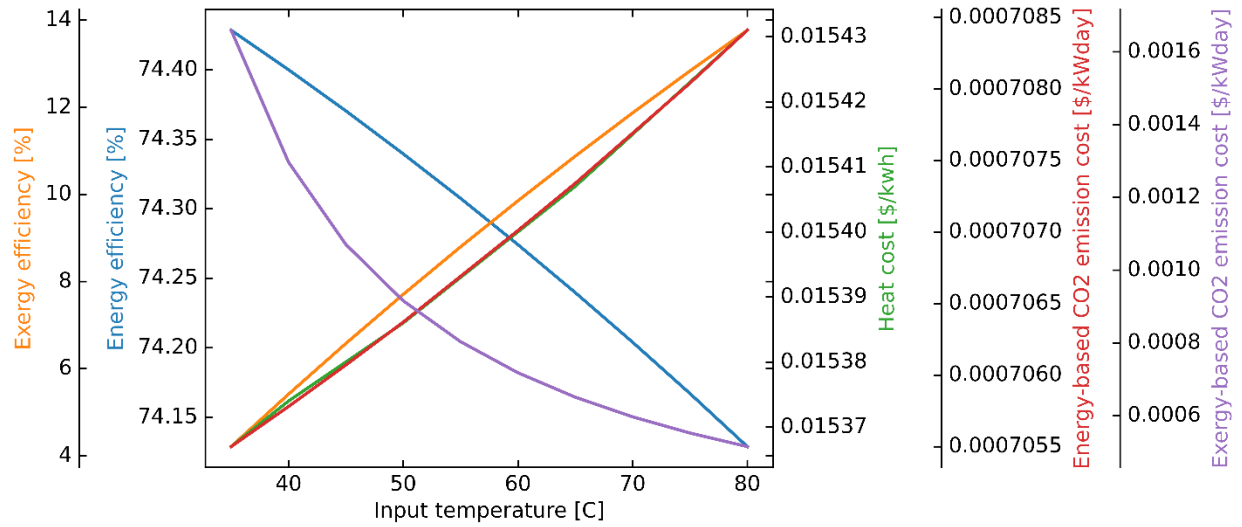


Figure 14: The variation of energy efficiency, exergy efficiency, heat cost, energy-based carbon dioxide emission cost and exergy-based carbon dioxide emission cost by input temperature of fluid

Figure 14 illustrates the variation of energy efficiency, exergy efficiency, heat cost, energy-based CO_2 emission cost and exergy-based CO_2 emission cost by input temperature of fluid. The energy efficiency is descending by increasing the input temperature, since the temperature difference between fluid and surrounding will be descending and subsequently the heat cost will be increasing. One of the exergy destruction reasons is temperature gap between hot and cold sources. Due to decreasing the temperature difference, the exergy destruction is decreasing that causes to elevate the exergy efficiency.

Figure 15 depicts the variation of energy efficiency, exergy efficiency, heat cost, energy-based CO_2 emission cost and exergy-based CO_2 emission cost by annulus pressure between absorber tube diameter and glass envelope. Energy and exergy efficiency curves are coincided by increasing the pressure since their slopes are equal together based on related y-axis scales. By increasing the pressure, the heat transfer convection will be more substantial as heat loss. Increasing heat loss term in the efficiency relations causes to decrease them. It is obvious that a fluid with negligible pressure tends to eliminate heat transfer convection.

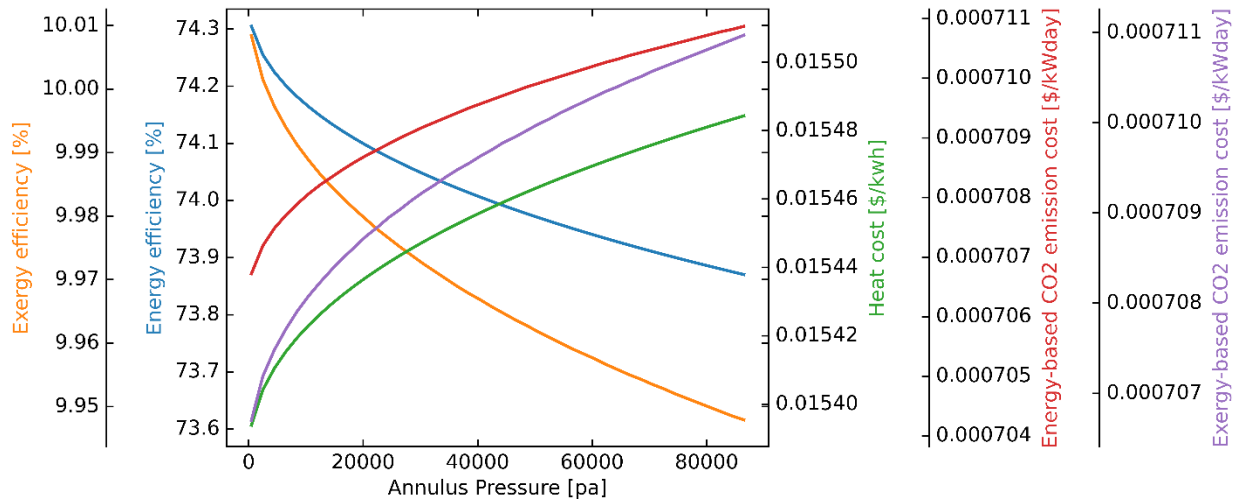


Figure 15: The variation of energy efficiency, exergy efficiency, heat cost, energy-based carbon dioxide emission cost and exergy-based carbon dioxide emission cost by annulus pressure between receiver tube diameter and glass pip

Figure 16 illustrates the variation of energy efficiency, exergy efficiency, heat cost, energy-based CO_2 emission cost and exergy-based CO_2 emission cost by the length of collector. The efficiencies are increasing with the length. By increasing the length, ascending in heat gain is more than gained solar radiation. The heat cost is decreasing. The reason is that regarding to heat cost equation, by ascending the length of PTSC, the heat gain rate is increased more than the numerator of heat cost equation. The exergy efficiency is ascending, although the difference in temperature between heat sources and pressure term in exergy efficiency cause dissipating exergy, why the heat gain rate term is dominant over the mentioned terms.

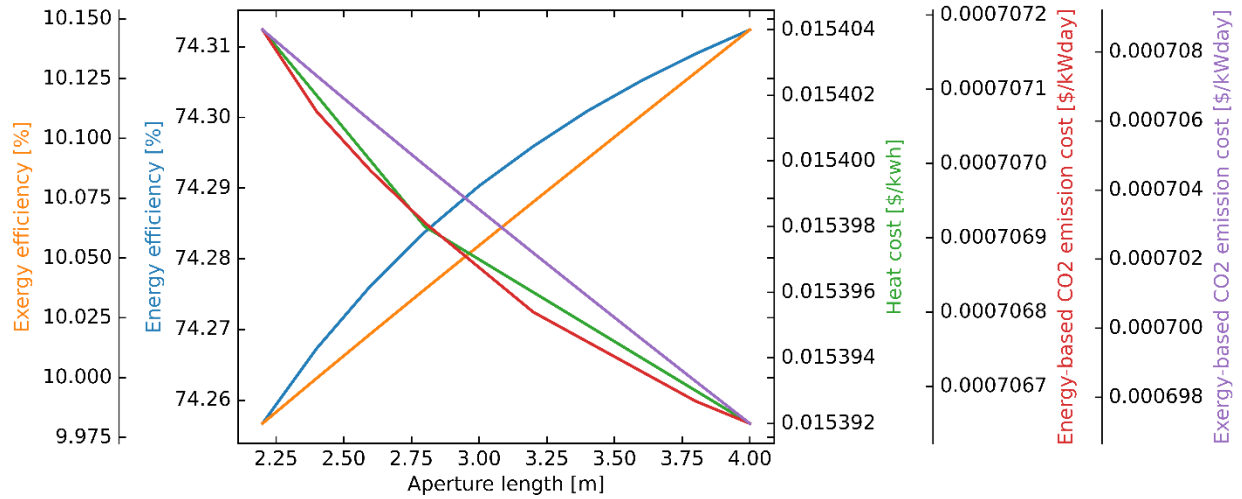


Figure 16: The variation of energy efficiency, exergy efficiency, heat cost, energy-based carbon dioxide emission cost and exergy-based carbon dioxide emission cost by the length of collector

Figure 17 shows the variation of energy efficiency, exergy efficiency, heat cost, energy-based CO_2 emission cost and exergy-based CO_2 emission cost by the width of collector. Similar to the variation of length, by increasing the length, the efficiencies are ascending and the heat cost function is descending. Furthermore, the reasons are the same based on thermal analysis in assessed bounds.

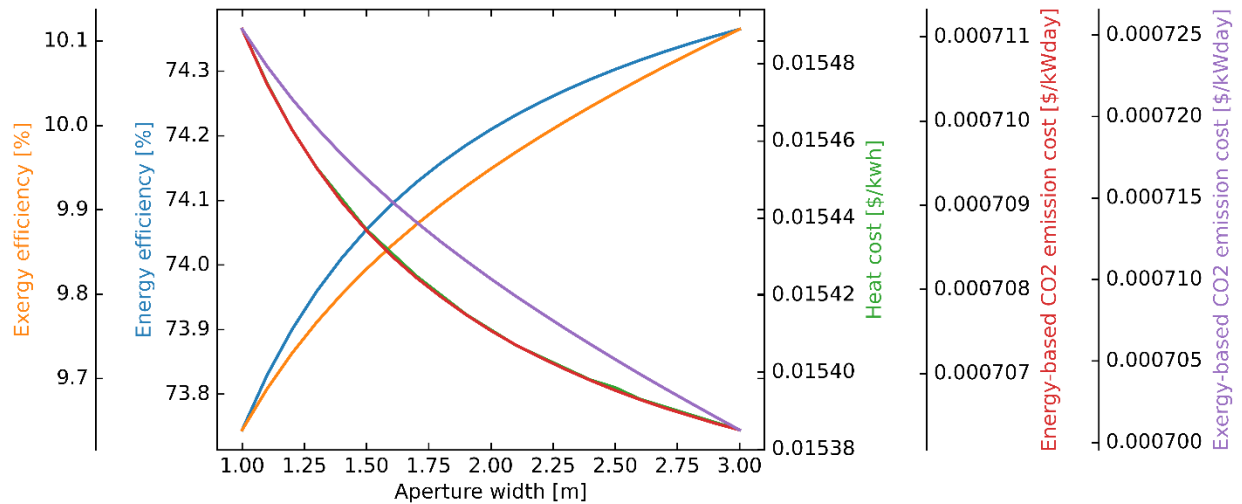


Figure 17: The variation of energy efficiency, exergy efficiency, heat cost, energy-based carbon dioxide emission cost and exergy-based carbon dioxide emission cost by the width of collector

The energy efficiency, exergy efficiency, heat cost, energy-based CO_2 emission cost and exergy-based CO_2 emission cost are calculated and depicted

to the various presented categorical variables in Figure 18, Figure 19, Figure 20, Figure 21, Figure 22.

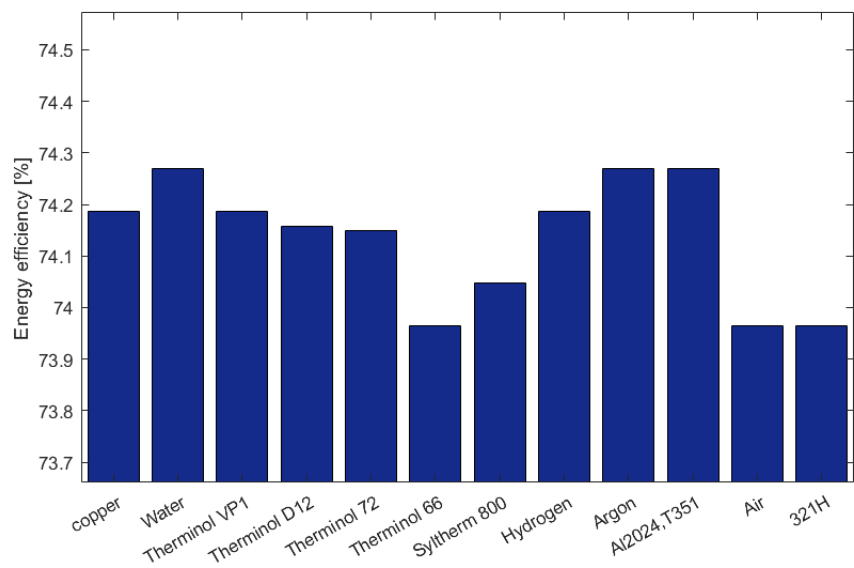


Figure 18: The energy efficiency for the various categorical variables

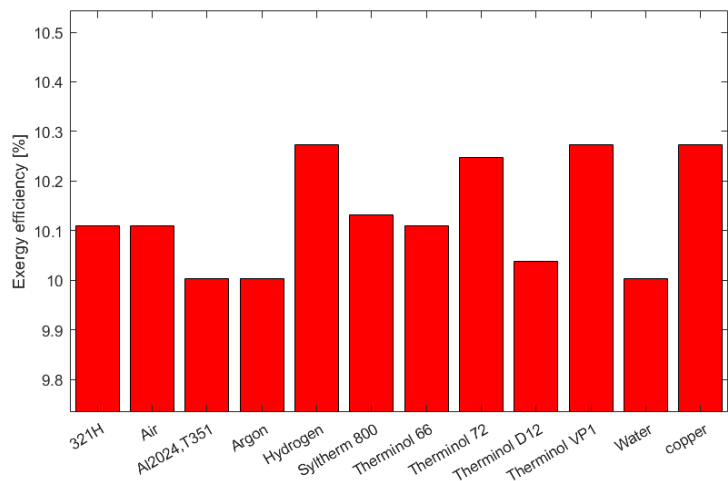


Figure 19: The exergy efficiency for the various categorical variables

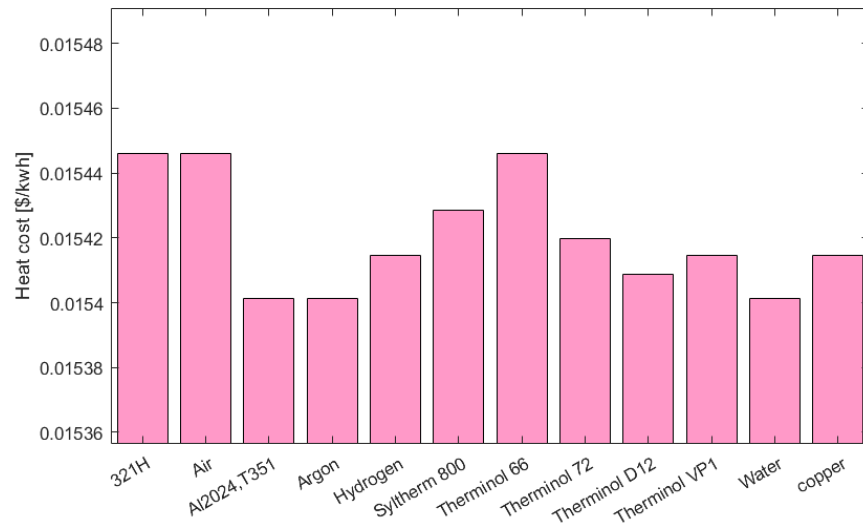


Figure 20: The heat cost for the various categorical variables

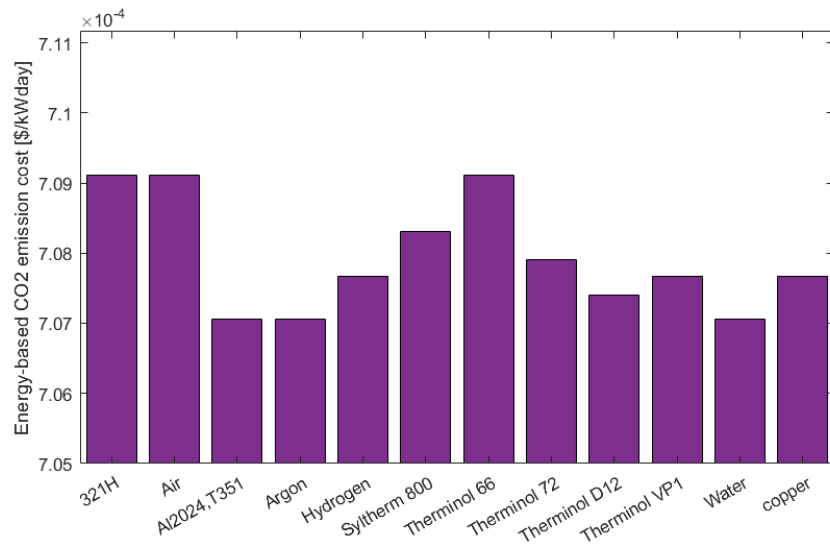


Figure 21: The energy-based carbon dioxide emission cost for the various categorical variables

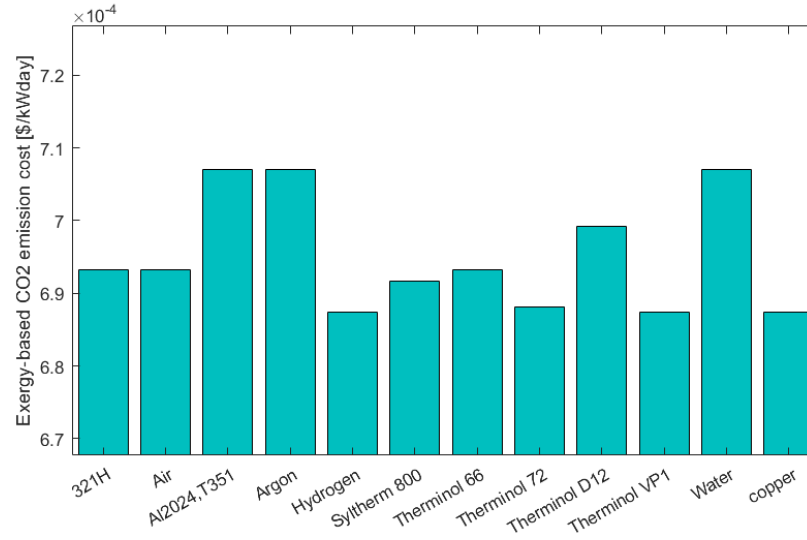


Figure 22: The exergy-based carbon dioxide emission cost for the various categorical variables

4.6. sensitivity analysis

As a result of utilizing the proposed machine learning approach, a sensitivity analysis of all continuous and categorical variables is extracted. Figure 23, Figure 24, and Figure 25 depict the importance of each input on a percentage scale. According to sensitivity analysis of energy efficiency, exergy efficiency, and heat cost function, the most important variables are aperture width, input temperature, and inner diameter of the absorber.

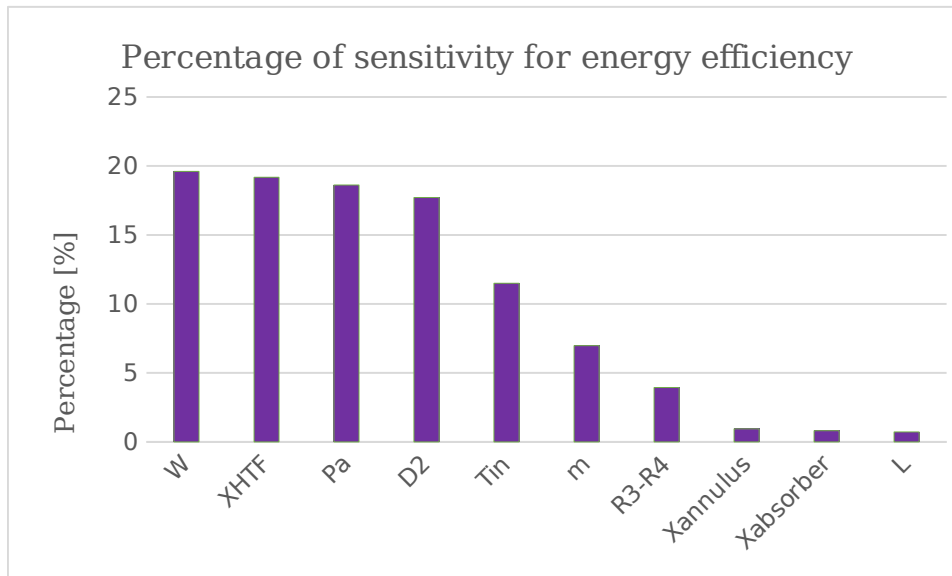


Figure 23: Percentage of sensitivity for energy efficiency for each input variable

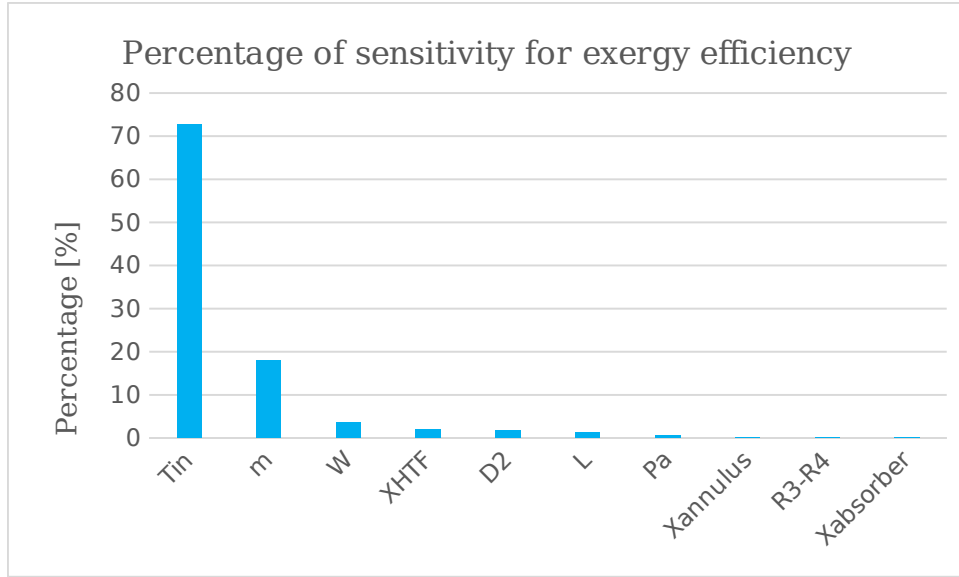


Figure 24: Percentage of sensitivity for exergy efficiency for each input variable

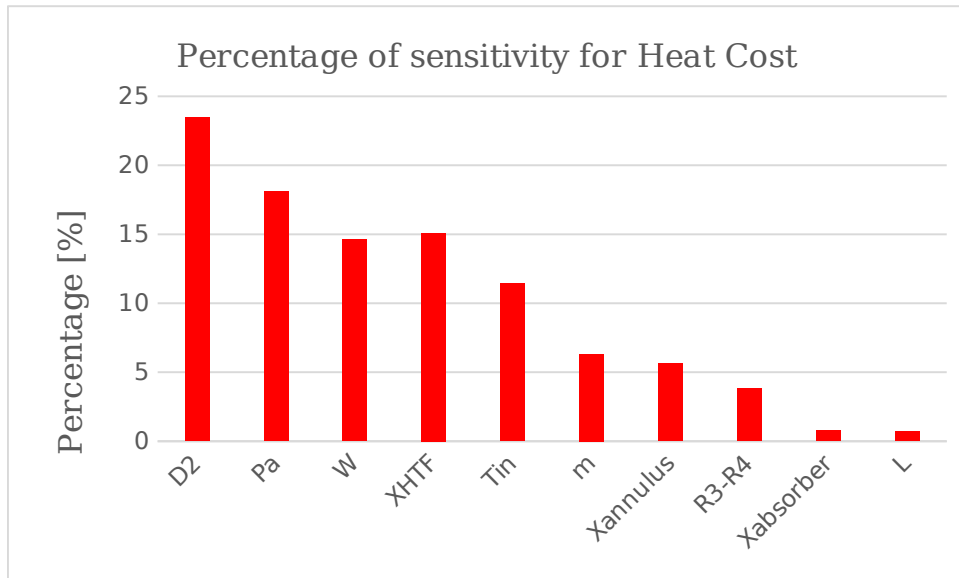


Figure 25: Percentage of sensitivity for heat cost function for each input variable

4. Conclusion

The present study provided a prospective comprehensive approach to dealing with complex problems and obtaining quick responses from high-time solution problems by applying an appropriate machine learning method for academic research and industrial applications. The article includes an investigation of a 4E analysis and optimization of a complex renewable energy system with machine learning, which needs to solve multiple unknowns and multiple equations with non-

linear terms. Through the proposed machine learning approach, assessing various inputs and variables to gain optimum conditions is provided. In this respect, after generating a comprehensive code for 4E analysis of a renewable energy system, validating with reference [52], obtaining proportionate inputs and outputs data and scaling, and providing a developed code to model an accurate machine learning model through the presented prospective approach, the considerable following consequences resulted:

- ✓ A comprehensive and prospective detailed approach of machine learning associated with complex and high-time solution engineering problems was proposed and discussed in detail.
- ✓ The proposed supervised machine learning approach utilized through a complex renewable energy system for a PTSC
- ✓ After training the machine learning model from the proper inputs and outputs data under governing the presented non-linear constraints, dealing with analysis, obtaining quick solutions and feedback, and optimization with low time was gained and the problem transposed from a cumbersome complex problem to a simplified and convenient problem
- ✓ Utilizing the presented approach and the trained machine learning model for optimization revealed the best options for categorical inputs and continuous variables up to 1143 times faster process through a substantially more convenient and predictable method. The categorical variables including water for HTF, copper for absorber type and argon for annulus gas type and the obtained values for continuous inputs are 0.014 m for inner diameter, 0.0074 m for distance between inner and outer pipes, 0.31214 kg/s for mass flow rate, 60.7 °C for input HTF temperature and 0 pa for annulus gas pressure. The related optimum objective function resulted in 74.27 % for energy efficiency, 10.003 % for exergy efficiency, 0.0154 (\$/kWh) 7.07057×10^{-4} \$/kWhday for energy-based CO_2 emission cost and 7.07048×10^{-4} \$/kWhday for exergy-based CO_2 emission cost.
- ✓ Furthermore, it is possible in a substantially more convenient and quick way for the simplified problem by machine learning model to perform post-processing. Thus, a comprehensive parametric investigations was illustrated for all input variables and objective functions in multi-scale depictions which assess the trends and turning points.
- ✓ In addition, a sensitivity analysis of variables is extracted from the trained machine learning model for objective functions, including energy efficiency, exergy efficiency and heat cost function.

| Nomenclature | | | |
|---------------------|--|--------------------------|---|
| A | Surface area of greenhouse (m^2) | <i>Abs</i> | Absorber |
| D | Diameter of pip | <i>Ch</i> | Chemical |
| C_f | unit cost of fuel (\$ kg ⁻¹) | DE | Direct energy |
| \dot{m}_{fuel} | the fuel mass flow rate (kg s ⁻¹) | IDE | Indirect energy |
| c | Unit cost (\$/kg) | <i>CC</i> | Combustion chamber |
| C_p | Specific heat (kJ/kg K) | <i>WF</i> | working fluid |
| \dot{C} | Cost rate (\$/s) | <i>Cond</i> | Condenser |
| \dot{C}_{env} | Environmental cost rate (\$ h ⁻¹) | <i>e</i> | Exit |
| c_{CO_2} | Unit cost of carbon dioxide (\$ kg ⁻¹) | <i>Gen</i> | Generator |
| f | friction factor | <i>Int</i> | Intercooler |
| F | activation function and the hidden layer's outputs | $LW_{l,s}$ | coefficients of the connection weights between the hidden layer |
| a_j | feed the output layer's neuron | $b_{2(l)}$ | bias by corresponding to the neuron in the output layer |
| \dot{m}_{CO_2} | carbon dioxide emission mass flow rate (kg s ⁻¹) | n | Required sample size |
| d | Distance of objective function values from reference point | <i>Pr</i> | Prandtel number |
| ex | Specific exergy (kJ/kg) | \dot{Ex} | Exergy rate (kW) |
| g | Constant gravity | \dot{Ex}_D | Exergy destruction rate (kW) |
| $f_{i,j}^i$ | Value of i th objective function | | |
| F_p | Partition function | <i>Subscripts</i> | |
| h | Specific enthalpy (kJ/kg) | 0 | Ambient condition |
| i | Interest rate | <i>In</i> | Inlet |
| L | Greenhouse length | <i>Com</i> | Compressor |
| \dot{m} | Mass flow rate (kg/s) | <i>Out</i> | Outlet |
| n | System life time | <i>ph</i> | physical |
| N | Operating years | <i>Ref</i> | Reference |

| | | | |
|------------|--|-----------------------------|--------------------------------------|
| P | Pressure (kPa, MPa) | SS | Strong solution |
| \dot{Q} | Heat transfer rate (kW) | Tur | Turbine |
| \dot{R} | required carbon dioxide rate for a greenhouse per unit of area | WS | Weak solution |
| s | Specific entropy (kJ/kg K) | <i>Greek Symbols</i> | |
| Nu | Nusselt number ζ | ε | Heat exchanger effectiveness |
| k | Conductivity | φ | Maintenance factor |
| T | Temperature (°C) | Φ_{eq} | Equivalence ratio of fuel |
| w | Weight of units | η | Efficiency (%) |
| Wi | Greenhouse width | ρ | Energy function |
| \dot{W} | Work production rate (kW) | <i>Abbreviations</i> | |
| X | Mass fraction | ORC | Organic Rankin Cycle |
| Z | Cost (\$) | CRF | Capital recovery factor |
| \dot{Z} | Cost rate (\$/s) | HHV | High Heating Value |
| ΔH | Change in enthalpy (kJ) | GA | Genetic algorithm |
| ΔS | Change in entropy (kJ/K) | HE | Heat exchanger |
| | | HTF | Heat Transfer Fluid |
| | | CCH | Combined Cooling, Heating, and Power |
| | | CI | Cost index |
| | | DBN N | Deep Belief Neural Network |
| | | GH | Greenhouse |
| | | GT | Gas turbine |
| | | LHV | Low Heating Value |
| ΔT | temperature difference (°C) | ARC | Absorption Refrigerant Cycle |
| | | COP | Coefficient of Performance |
| | | CRF | Capital recovery factor |

References

- [1] Ajbar W, Parrales A, Cruz-Jacobo U, Conde-Gutiérrez RA, Bassam A, Jaramillo OA, et al. The multivariable inverse artificial neural network combined with GA and PSO to improve the performance of solar parabolic trough collector. *Appl Therm Eng* 2021;189. <https://doi.org/10.1016/j.applthermaleng.2021.116651>.
- [2] Boukelia TE, Mecibah MS. Parabolic trough solar thermal power plant: Potential, and projects development in Algeria. *Renew Sustain Energy Rev* 2013;21:288–97. <https://doi.org/10.1016/j.rser.2012.11.074>.
- [3] El Ghazzani B, Martinez Plaza D, Ait El Cadi R, Ihlal A, Abnay B, Bouabid K. Thermal plant based on parabolic trough collectors for industrial process heat generation in Morocco. *Renew Energy* 2017;113:1261–75. <https://doi.org/10.1016/j.renene.2017.06.063>.
- [4] Fuqiang W, Ziming C, Jianyu T, Yuan Y, Yong S, Linhua L. Progress in concentrated solar power technology with parabolic trough collector system: A comprehensive review. *Renew Sustain Energy Rev* 2017;79:1314–28. <https://doi.org/10.1016/j.rser.2017.05.174>.
- [5] Ehyaei MA, Ahmadi A, El M, Assad H, Hachicha AA, Said Z. Energy, exergy and economic analyses for the selection of working fluid and metal oxide nanofluids in a parabolic trough collector 2019. <https://doi.org/10.1016/j.solener.2019.05.046>.
- [6] Fernández-García A, Zarza E, Valenzuela L, Pérez M. Parabolic-trough solar collectors and their applications. *Renew Sustain Energy Rev* 2010;14:1695–721. <https://doi.org/10.1016/j.rser.2010.03.012>.
- [7] Ghritlahre HK, Prasad RK. Application of ANN technique to predict the performance of solar collector systems - A review. *Renew Sustain Energy Rev* 2018;84:75–88. <https://doi.org/10.1016/J.RSER.2018.01.001>.
- [8] Rabl A, Bendt P, Gaul HW. Optimization of parabolic trough solar collectors. *Sol Energy* 1982;29:407–17. [https://doi.org/10.1016/0038-092X\(82\)90077-9](https://doi.org/10.1016/0038-092X(82)90077-9).
- [9] Haykin S, Lippmann R. Neural networks, a comprehensive foundation. *Int J Neural Syst* 1994;5:363–4.
- [10] Nadhir Ab Wahab M, Nefti-Meziani S, Atyabi A. A Comprehensive Review of Swarm Optimization Algorithms 2015. <https://doi.org/10.1371/journal.pone.0122827>.
- [11] Ghasemian E, Ehyaei • M A, Ehyaei MA. (8) Evaluation and optimization of organic Rankine cycle (ORC) with algorithms NSGA-II, MOPSO, and MOEA for eight coolant fluids Turbine power production (kW) (8). *Int J Energy Environ Eng* 2018;9:39–57. <https://doi.org/10.1007/s40095-017-0251-7>.
- [12] Hosseinalipour SM, Rostami A, Shahriari G. Numerical study of circumferential temperature difference reduction at the absorber tube of parabolic trough direct steam generation collector by inserting a twisted tape in superheated region. *Case Stud Therm Eng*

- 2020;21:100720. <https://doi.org/10.1016/j.csite.2020.100720>.
- [13] Hoseinzadeh H, Kasaeian A, Shafii MB. Exergoeconomic optimization and sensitivity analysis of a commercial parabolic trough collector for the climate of Tehran, Iran. *Energy Sci Eng* 2019;7:2950–65. <https://doi.org/10.1002/ese3.472>.
 - [14] Moosavian SF, Borzuei D, Ahmadi A. Energy, exergy, environmental and economic analysis of the parabolic solar collector with life cycle assessment for different climate conditions. *Renew Energy* 2021;165:301–20. <https://doi.org/10.1016/j.renene.2020.11.036>.
 - [15] Chitgar N, Moghimi M. Design and evaluation of a novel multi-generation system based on SOFC-GT for electricity, fresh water and hydrogen production. *Energy* 2020;197:117162. <https://doi.org/10.1016/j.energy.2020.117162>.
 - [16] Mehrenjani JR, Gharehghani A, Sangesaraki AG. Machine learning optimization of a novel geothermal driven system with LNG heat sink for hydrogen production and liquefaction. *Energy Convers Manag* 2022;254:115266. <https://doi.org/10.1016/j.enconman.2022.115266>.
 - [17] Nasrabadi AM, Moghimi M. Energy analysis and optimization of a biosensor-based microfluidic microbial fuel cell using both genetic algorithm and neural network PSO. *Int J Hydrogen Energy* 2022;47:4854–67. <https://doi.org/10.1016/j.ijhydene.2021.11.125>.
 - [18] Nasrabadi AM, Malaie O, Moghimi M, Sadeghi S, Hosseinalipour SM. Deep learning optimization of a combined CCHP and greenhouse for CO₂ capturing; case study of Tehran. *Energy Convers Manag* 2022;267:115946. <https://doi.org/10.1016/j.enconman.2022.115946>.
 - [19] Mehrenjani JR, Gharehghani A, Nasrabadi AM, Moghimi M. Design, modeling and optimization of a renewable-based system for power generation and hydrogen production. *Int J Hydrogen Energy* 2022;47:14225–42. <https://doi.org/10.1016/j.ijhydene.2022.02.148>.
 - [20] Duffie JA, Beckman WA. *Solar engineering of thermal processes*. John Wiley & Sons; 2013.
 - [21] Shamoushaki M, Ghanatir F, Ehyaei MA, Ahmadi A. Exergy and exergoeconomic analysis and multi-objective optimisation of gas turbine power plant by evolutionary algorithms. Case study: Aliabad Katoul power plant. *Int J Exergy* 2017;22:279–307. <https://doi.org/10.1504/IJEX.2017.083160>.
 - [22] Munson BR, Gerhart PM, Gerhart AL, Hochstein JI, Young DF, Okiishi TH (Theodore H. Munson, Young, and Okiishi's *Fundamentals of fluid mechanics* n.d.:11.
 - [23] Jehring L, Bejan, A., *Advanced Engineering Thermodynamics*. New York etc., John Wiley & Sons 1988. XXIII, 758 pp. ISBN 0-471-83043-7. *ZAMM - J Appl Math Mech / Zeitschrift Für Angew Math Und Mech* 1992;72:320–320. <https://doi.org/10.1002/ZAMM.19920720803>.
 - [24] Gnielinski V. *New equations for heat and mass transfer in turbulent pipe and channel flow*. Undefined 1976.
 - [25] Incropera FP, DeWitt DP. *Fundamentals of heat and mass transfer*

- 1990.
- [26] Ratzel AC, Hickox CE, Gartling DK. Techniques for Reducing Thermal Conduction and Natural Convection Heat Losses in Annular Receiver Geometries. *J Heat Transfer* 1979;101:108-13. <https://doi.org/10.1115/1.3450899>.
 - [27] Ouagued M, Khellaf A. Simulation of the Temperature and Heat Gain by Solar Parabolic Trough Collector in Algeria. *Int J Phys Math Sci* 2012;6:746-52. <https://doi.org/10.5281/ZENODO.1063324>.
 - [28] Petela R. Exergy of heat radiation 1964.
 - [29] Landsberg P, on JM-IC, 1976 undefined. Thermodynamic constraints, effective temperatures and solar cells. *UiAdsabsHarvardEdu* n.d.
 - [30] Press WH. Theoretical maximum for energy from direct and diffuse sunlight. *Nat* 1976 264:5588 1976;264:734-5. <https://doi.org/10.1038/264734a0>.
 - [31] Badescu V. How much work can be extracted from diluted solar radiation? *Sol Energy* 2018;170:1095-100. <https://doi.org/10.1016/J.SOLENER.2018.05.094>.
 - [32] Bellos E, Tzivanidis C. A detailed exergetic analysis of parabolic trough collectors. *Energy Convers Manag* 2017;149:275-92. <https://doi.org/10.1016/J.ENCONMAN.2017.07.035>.
 - [33] Caliskan H. Energy, exergy, environmental, enviroeconomic, exergoenvironmental (EXEN) and exergoenvironoeconomic (EXENEC) analyses of solar collectors. *Renew Sustain Energy Rev* 2017;69:488-92. <https://doi.org/10.1016/J.RSER.2016.11.203>.
 - [34] Kalogirou SA. Solar thermal collectors and applications. *Prog Energy Combust Sci* 2004;30:231-95. <https://doi.org/10.1016/J.PECS.2004.02.001>.
 - [35] Frangopoulos CA. Thermo-economic functional analysis and optimization. *Energy* 1987;12:563-71. [https://doi.org/10.1016/0360-5442\(87\)90097-1](https://doi.org/10.1016/0360-5442(87)90097-1).
 - [36] Silveira JL, Tuna CE. Thermoeconomic analysis method for optimization of combined heat and power systems. Part I. *Prog Energy Combust Sci* 2003;29:479-85. [https://doi.org/10.1016/S0360-1285\(03\)00041-8](https://doi.org/10.1016/S0360-1285(03)00041-8).
 - [37] Palenzuela P, Alarcón-Padilla DC, Zaragoza G. Large-scale solar desalination by combination with CSP: Techno-economic analysis of different options for the Mediterranean Sea and the Arabian Gulf. *Desalination* 2015;366:130-8. <https://doi.org/10.1016/J.DESAL.2014.12.037>.
 - [38] Faizal M, Saidur R, Mekhilef S, Hepbasli A, Mahbubul IM. Energy, economic, and environmental analysis of a flat-plate solar collector operated with SiO₂ nanofluid. *Clean Technol Environ Policy* 2015;17:1457-73. <https://doi.org/10.1007/s10098-014-0870-0>.
 - [39] Caliskan H. Novel approaches to exergy and economy based enhanced environmental analyses for energy systems. *Energy Convers Manag* 2015;89:156-61. <https://doi.org/10.1016/j.enconman.2014.09.067>.

- [40] Varun, Bhat IK, Prakash R. LCA of renewable energy for electricity generation systems-A review. *Renew Sustain Energy Rev* 2009;13:1067-73. <https://doi.org/10.1016/j.rser.2008.08.004>.
- [41] Å BKS. Valuing the greenhouse gas emissions from nuclear power : A critical survey 2008;36:2950-63. <https://doi.org/10.1016/j.enpol.2008.04.017>.
- [42] Caliskan H. Energy, exergy, environmental, enviroeconomic, exergoenvironmental (EXEN) and exergoenvironmental (EXENEC) analyses of solar collectors. *Renew Sustain Energy Rev* 2017;69:488-92. <https://doi.org/https://doi.org/10.1016/j.rser.2016.11.203>.
- [43] Deniz E, Çınar S. Energy, exergy, economic and environmental (4E) analysis of a solar desalination system with humidification-dehumidification. *Energy Convers Manag* 2016;126:12-9. <https://doi.org/https://doi.org/10.1016/j.enconman.2016.07.064>.
- [44] Khorasanizadeh H, Mohammadi K. Introducing the best model for predicting the monthly mean global solar radiation over six major cities of Iran. *Energy* 2013;51:257-66. <https://doi.org/https://doi.org/10.1016/j.energy.2012.11.007>.
- [45] den Elzen MGJ, Hof AF, Mendoza Beltran A, Grassi G, Roelfsema M, van Ruijven B, et al. The Copenhagen Accord: abatement costs and carbon prices resulting from the submissions. *Environ Sci Policy* 2011;14:28-39. <https://doi.org/https://doi.org/10.1016/j.envsci.2010.10.010>.
- [46] Saadon S, Gaillard L, Menezo C, Giroux-Julien S. Exergy, exergoeconomic and enviroeconomic analysis of a building integrated semi-transparent photovoltaic/thermal (BISTPV/T) by natural ventilation. *Renew Energy* 2020;150:981-9. <https://doi.org/https://doi.org/10.1016/j.renene.2019.11.122>.
- [47] ICT Institute | AI, Machine Learning and neural networks explained n.d. <https://ictinstitute.nl/ai-machine-learning-and-neural-networks-explained/> (accessed September 10, 2022).
- [48] Mathworks. PDE Toolbox: User's Guide 2018.
- [49] Foundations of neural networks, fuzzy systems, and knowledge engineering. *Choice Rev Online* 1997;35:35-0330-35-0330. <https://doi.org/10.5860/CHOICE.35-0330>.
- [50] Despagne F. Neural networks in multivariate calibration. *Analyst* 1998;123. <https://doi.org/10.1039/A805562I>.
- [51] [52] A. Bassani, R.A. Conde-Gutierrez, J. Castillo, G. Laredo, J.A. Hernandez, Direct neural network modeling for separation of linear and branched paraffins by adsorption process for gasoline octane number improvement, *Fuel* (2014), <https://doi.org/10.1016/j.fue1.2014.01.080>. - Google Search n.d. <https://www.google.com/search?client=firefox-b-d&q=%5B52%5D+A.+Bassani%2C+R.A.+Conde-Gutierrez%2C+J.+Castillo%2C+G.+Laredo%2C+J.A.+Hernandez%2C+Direct+neural+network+modeling+for+separation+of+linear+>

and+branched+paraffins+by+adsorption+process+for+gasoline+octane+number+improvement%2C+Fuel+%282014%29%2C+https%3A%2F%2F+doi.org%2F10.1016%2Fj.fue1.2014.01.080. (accessed September 11, 2022).

- [52] Bassam A, Conde-Gutierrez RA, Castillo J, Laredo G, Hernandez JA. Direct neural network modeling for separation of linear and branched paraffins by adsorption process for gasoline octane number improvement. *Fuel* 2014;Complete:158-67. <https://doi.org/10.1016/J.FUEL.2014.01.080>.
- [53] Bertrand TF, Papadakis G, Lambrinos G, Frangoudakis A. Fluid selection for a low-temperature solar organic Rankine cycle. Elsevier n.d. <https://doi.org/10.1016/j.applthermaleng.2008.12.025>.
- [54] Forristall R. Heat Transfer Analysis and Modeling of a Parabolic Trough Solar Receiver Implemented in Engineering Equation Solver Heat Transfer Analysis and Modeling of a Parabolic Trough Solar Receiver Implemented in Engineering Equation Solver. 2003.